Oceanographic variability in Cumberland Bay, South Georgia, and its implications for glacier retreat

Joanna C. Zanker[1,2], Emma. Young[1], Paul. R. Holland[1], Ivan D. Haigh[2], Paul Brickle[3]

[1]British Antarctic Survey, Cambridge, UK. [2]Ocean and Earth Science, National Oceanography Centre, University of Southampton, Southampton, UK. [3]South Atlantic Environmental Research Institute, Stanley, FI.

Corresponding author: Joanna C. Zanker (joazan@bas.ac.uk)

Key Points:

- Observational data and a new high-resolution model are combined to describe oceanographic variability in Cumberland Bay, South Georgia.
- We show that the properties of buoyancy-driven outflow plumes are sensitive to bathymetry and drive spatial differences between fjord arms.
- We highlight that the presence of a postulated inner sill may be a key factor in the observed rapid glacier retreat.

Abstract

South Georgia is a heavily glaciated sub-Antarctic island in the Southern Ocean. Cumberland Bay is the largest fjord on the island, split into two arms, each with a large marine-terminating glacier at the head. Although these glaciers have shown markedly different retreat rates over the past century, the underlying drivers of such differential retreat are not yet understood. This study uses observations and a new high-resolution oceanographic model to characterize oceanographic variability in Cumberland Bay and to explore its influence on glacier retreat. While observations indicate a strong seasonal cycle in temperature and salinity, they reveal no clear hydrographic differences that could explain the differential glacier retreat. Model simulations suggest the subglacial outflow plume dynamics and fjord circulation are sensitive to the bathymetry adjacent to the glacier, though this does not provide persuasive reasoning for the asymmetric glacier retreat. The addition of a postulated shallow inner sill in one fjord arm, however, significantly changes the water properties in the resultant inner basin by blocking the intrusion of colder, higher salinity waters at depth. This increase in temperature could significantly increase submarine melting, which is proposed as a possible contribution to the different rates of glacier retreat observed in the two fjord arms. This study represents the first detailed description of the oceanographic variability of a sub-Antarctic island fjord, highlighting the sensitivity of fjord oceanography to bathymetry. Notably, in fjords systems where temperature decreases with depth, the presence of a shallow sill has the potential to accelerate glacier retreat.

Plain Language Summary

Cumberland Bay, a fjord on the sub-Antarctic island of South Georgia, is split into two arms, each with a large marine-terminating glacier. One of these glaciers is retreating much faster than the other, possibly due to differences in oceanography between the arms. Here, we investigate how the oceanography in Cumberland Bay varies seasonally and with the seabed depth by using oceanographic data and numerical ocean simulations. We find that the properties of buoyant plumes, which arise from meltwater entering the ocean from beneath the glacier, are sensitive to the seabed depth near the glaciers, resulting in strong differences in ocean flow between the fjord arms. Assuming higher ocean temperatures increase glacier melting, we find that the presence of a near-glacier shallow sill likely increases melting by blocking deeper, colder waters and trapping warmer surface waters close to the glacier. As a shallow sill is likely to be present near

the rapidly retreating glacier only, this result offers a persuasive explanation for the observed glacier retreat. Understanding the variability in oceanography and glacier retreat is important as they directly impact the marine ecosystem at South Georgia by influencing the availability of nutrients for primary production and food availability for higher predators.

1 Introduction

Fjords are a common feature of high-latitude coastlines and have high biological productivity. In the Arctic, fjords are found in Alaska, Svalbard, and Greenland, for example. In the Southern Hemisphere, fjords are found in Patagonia, New Zealand, Antarctica, and on sub-Antarctic islands. High-latitude fjords are usually associated with seasonal sea ice and, in most cases, have a glacier terminating at the fjord head (Cottier et al., 2010). Fjord circulation directly governs the stability of tidewater glaciers (Cottier et al., 2010), frontal ablation of which directly contributes to sea-level rise (Benn et al., 2017).

Marine ecosystems in fjords support large colonies of higher predators such as sea birds and marine mammals (Ward, 1989; Węsławski et al., 2000), while open ocean and on-shelf phytoplankton blooms may also rely on the transport of nutrients circulated by nearby fjords from upwelling and terrestrial sources via glacial runoff (Holmes et al., 2019; Węsławski et al., 2000). Fjords are also important spawning grounds for fish (Everson et al., 2001). Recruitment and retention of fish larvae are controlled by fjord circulation and shelf exchange, an understanding of which is vital for the management of local fisheries (Everson, 1992). In our changing climate, frontal ablation of tidewater glaciers is expected to increase (Christoffersen et al., 2011; Mortensen et al., 2011; Straneo et al., 2010), the composition and extent of phytoplankton blooms are expected to change substantially (Sommer & Lengfellner, 2008; Winder & Sommer, 2012) and the changes in fjord circulation are likely to impact a diversity of ecosystem responses, such as fish larvae retention (Wesławski et al., 2011). Therefore, understanding fjord systems is crucial.

In this paper, we focus on South Georgia, a sub-Antarctic island in the Southern Ocean, which is heavily glaciated and indented with fjords. The island lies in the path of the Antarctic Circumpolar Current (ACC), which flows unimpeded around the Southern Ocean, driven by strong westerly winds (Orsi et al., 1995). The Polar Front lies to the north of the island and the

Southern Antarctic Circumpolar Current Front (SACCF) loops anticyclonically around the island from the south before retroflecting to the east (Fig. 1a) (Meredith et al., 2005). While the island lies beyond the winter sea-ice limit, it does see the formation of intermittent seasonal pancake ice. Cumberland Bay, situated on the northeast coast, is the largest fjord on the island and is characterized by two arms, East Bay and West Bay (Fig 1a, green square). Cumberland East Bay (EB) is approximately 15 km long and 3-5 km wide, with a maximum depth of 270 m. Nordenskjöld Glacier terminates at the head of EB and there is a shallow inner basin with a prominent inner basin sill (Hodgson et al., 2014, Fig. 4). A deep outer basin sill marks the edge of the outer basin (Fig. 1c). Cumberland West Bay (WB) is approximately 18 km long and 2.5 - 5 km wide, with a maximum depth of 265 m. Neumayer Glacier terminates at the head of West Bay. The outer basin sill of WB is eroded towards the southern half of the fjord (Hodgson et al., 2014). Bathymetric surveys have not extended close enough to the glacier to identify an inner basin sill, though chart data (Admiralty Chart 3588, Approaches to Stromness and Cumberland Bay) include shallow points (~30 m) extending the width of WB in the area highlighted in Fig. 1c (white dashed lines). We believe these data indicate a sill, and for the remainder of this paper, this is referred to as the 'postulated' inner sill.

The individual behaviors of the glaciers have shown a high degree of variability (Cook et al., 2010; Gordon et al., 2008). Nordenskjöld Glacier showed little change in terminus position until recently, whereas satellite imagery tracking the terminus position of Neumayer Glacier shows a retreat of ~8 km between 1938 and 2020 (with further retreat in recent years) (Fig. 2). The WB postulated inner sill appears to have been a pinning point for Neumayer Glacier between ~ 1938 and 1983, before the onset of rapid retreat at a rate of ~ 200 m per year. Therefore, it is possible that once the glacier had retreated from the postulated inner sill into deeper water, the retreat has been a purely ice-dynamic response, and the glacier has not re-stabilized on another pinning point (Benn & Evans, 2014; Motyka et al., 2017). However, as the bathymetry is unknown around the postulated inner sill and beyond, it is possible that the intensification of ocean-driven melting may be playing a role in the rapid retreat.

Previous work has demonstrated that an increase in submarine melting may be a key driver of the observed increase in mass loss of tidewater glaciers in recent years, both directly through increased melt and indirectly by altering the ice front shape such that the rate of calving is increased (e.g., Luckman et al., 2015; O'Leary & Christoffersen, 2013). The melt rate is

approximately proportional to the difference between the temperature of the water and the ice freezing temperature (thermal driving) and the speed of the flow at the ice-ocean interface (boundary layer velocity) (Holland & Jenkins, 1999; Millgate et al., 2013). These quantities depend on the wider circulation regime within the fjord. Factors influencing the circulation regime include fjord-shelf exchange, atmospheric forcing, surface freshwater runoff, subglacial discharge, and fjord geometry, such as bathymetric sills (e.g., Bartholomaus et al., 2016; Boone et al., 2017; Catania et al., 2018; Cottier et al., 2010; Fraser & Inall, 2018; Hager et al., 2022; Mortensen et al., 2011). Fjord circulation patterns are complex, and there is a lack of clear understanding of how the interactions between these processes lead to glacier retreat, particularly in fjord systems where warm water overlays colder water, such as in Cumberland Bay. This temperature structure is unusual for high-latitude fjords, which are generally characterized by cold, fresh waters from ice sheet runoff overlaying warmer waters (Lin et al., 2018; Silvano et al., 2017).

Oceanic melting of tidewater glaciers is enhanced when subglacial discharge meets the ocean and rises as a buoyant plume in contact with the submarine ice face (Slater et al., 2015). Subglacial discharge arises from surface glacial meltwater that has been directed through moulins and crevasses on the ice surface to reach the bed and then fed through a system of subglacial channels towards the glacier's grounding line, along with direct basal glacier melt (Chu, 2014). The discharge enters the ocean and entrains ambient ocean water generating inflow at depth as it rises as a buoyant plume in contact with the ice (Jenkins, 2011). The plume reaches either neutral density or the ocean surface, resulting in a thick flow away from the glacier. The inflow and outflow generated by the subglacial discharge is known as buoyancy-driven circulation (Carroll et al., 2015; Straneo & Cenedese, 2015). The interaction between buoyancy-driven circulation and submarine sills has the potential to alter the water circulation and the heat available for melting at the submarine face, as the sill acts as a barrier to ocean currents (Hager et al., 2022; Holland & Jenkins, 1999). This interaction may give rise to spatial differences in fjord systems with multiple glaciers and complex bathymetry and is likely to change with the seasonally varying rate of subglacial discharge (Bartholomaus et al., 2016).

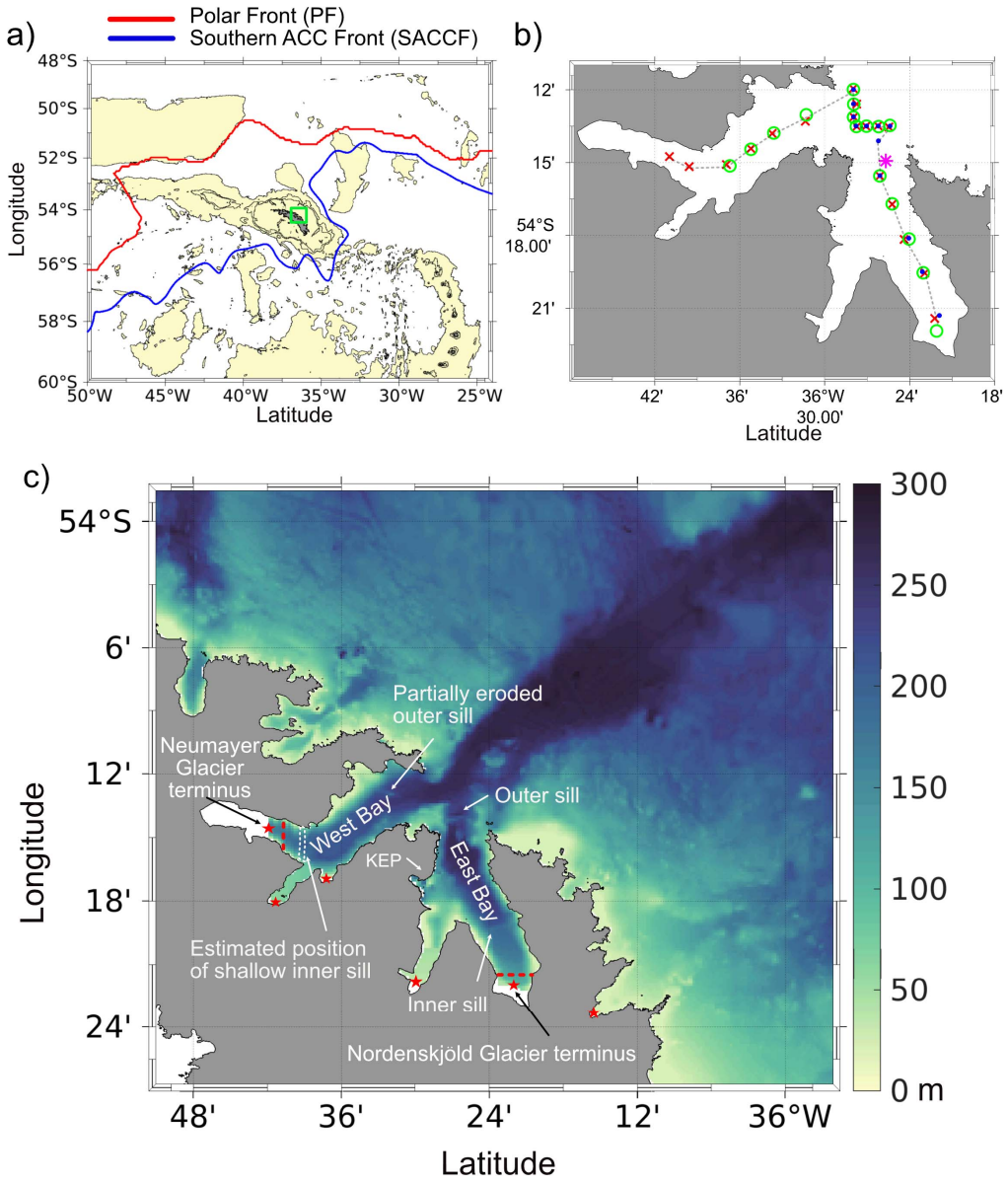

Figure 1. (a) Location of South Georgia in the Southern Ocean, with contours at 300, 1000, and 3000 m, and depths shallower than 3000 m shaded. Climatological locations of the Polar Front and Southern ACC Front are illustrated (Thorpe, 2001) and the location of Cumberland Bay is shown with the green square. (b) Positions of oceanographic surveys in Cumberland Bay from April 2012 (blue dots), February 2020 (green circles), November 2021 (red crosses), and January to November 2006 (pink star), and transect used for plotting data (grey dash line). (c) Cumberland Bay model domain, with bathymetry shaded (Hogg et al. 2016). Important bathymetric features are labelled, locations of glacier meltwater input are marked (red stars) and the locations of the cross-sections used for volume transport calculations are shown (red dashed

135 In this study, we use oceanographic observations from Cumberland Bay and a new high-
136 resolution ocean model (section 2) to address two main objectives. The first objective is to
137 describe the seasonal and spatial variability between the two fjord arms, providing the first
138 detailed study of this fjord system (section 3.1). The second objective is to take a first look at the
139 drivers of oceanographic variability that may influence glacier retreat, focusing on buoyancy-
140 driven outflow and the presence of the postulated submarine sill (section 3.2). We then assess the
141 limitations of the observations and modeling approach and discuss the implications of the results
142 for understanding the rate of glacier retreat (section 4).

143

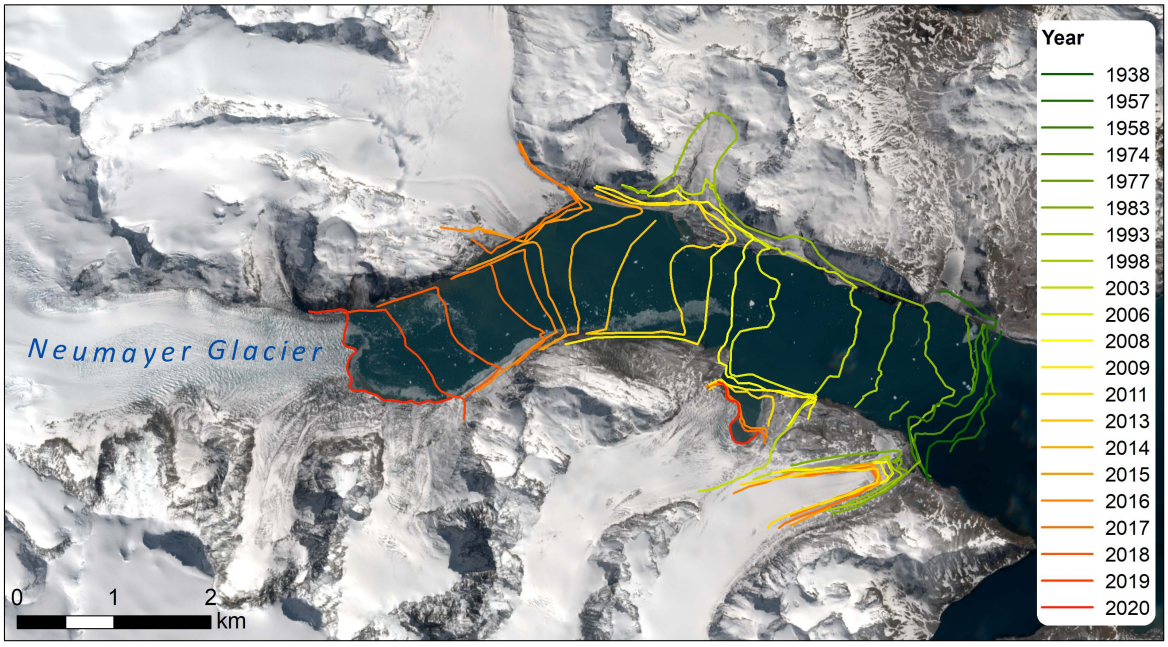

Figure 2. Image provided by the Mapping and Geographical Information Centre (MAGIC) at the British Antarctic Survey showing the terminus positions of Neumayer Glacier between 1938 and 2020.

2 Data and methods

2.1 Observations

Four datasets of Conductivity Temperature Depth (CTD) data for Cumberland Bay from 2000 - 2021 were collated. These data provide information on the temporal and spatial variability of temperature and salinity in Cumberland Bay, as well as a resource for model validation. Firstly, CTD data were collected with irregular temporal frequency from five points in Cumberland East Bay between 2001 and 2006 by staff at King Edward Point station, using a Sea-Bird E19 (Fig 1b, pink star). Data between 2004 and 2006 in the mouth of East Bay are chosen for analysis here, as these years and the location had the best temporal coverage. Secondly, opportunistic CTD data were collected in Cumberland Bay on the 18th of April 2012 (JR272A) with a Sea-Bird E32 carousel water sampler (Fig. 1b, blue dots). Thirdly, between the 24th and 25th of February 2020 (DY113), a CTD survey was conducted with a Sea-Bird 9+ (Fig. 1b, green circles). Finally, between the 9th and 14th of November 2021 (MV Pharos SG 12-21B), data were collected with a Valeport fastCTD (Fig. 1b, red crosses). Data were processed by removing outliers, averaging into 2 m bins, and converting from in-situ temperature and practical salinity to conservative temperature and absolute salinity, respectively.

2.2 Oceanographic model

2.2.1 Model setup

A high-resolution Cumberland Bay model was built using the Nucleus for European Modeling of the Ocean version 4.0.6 (NEMO4), which solves the three-dimensional hydrostatic equations of motion for an incompressible fluid under the Boussinesq approximation on a structured computational grid. The vertical coordinate is represented with 35 vertical levels arranged as partial-cell z-levels. The levels are gradually stretched to achieve higher resolution in the surface layer, with a grid spacing near the surface of ~1 m reducing to ~30 m at depth. The domain is chosen to ensure the open boundaries are sufficiently far from the main region of interest (Cumberland Bay) to limit their influence whilst allowing a good representation of variability in the wider shelf oceanography (Fig. 1c). Thus, the model domain extends to the shelf edge to the north, such that the maximum model depth does not exceed 300 m, and the

western and eastern boundaries are positioned to capture a portion of the adjacent coastline (Young et al., 2014). A horizontal grid spacing of 1/500^{o} latitude by 1/300^{o} longitude (~200 m) is chosen, with a resulting domain comprised of 280 by 240 grid cells in the horizontal. The resultant model is fine enough to resolve flows within Cumberland Bay whilst sufficiently computationally efficient for multi-year simulations.

NEMO4 uses the hydrostatic approximation, which saves considerably on computational expense. Although there are non-hydrostatic processes within the fjord, particularly over the sills, the effects are only likely to be resolved properly with a non-hydrostatic model if the horizontal grid spacing is significantly less than 100 m (Berntsen et al., 2009). However, a finer grid combined with the additional computational requirements of the non-hydrostatic solution would make the model too computationally expensive for multi-year simulations (Staalstrøm & Petter, 2016). A method for representing the subglacial plume using an offline model is described in section 2.2.4, which provides an efficient alternative for the representation of this non-hydrostatic process.

The model includes a free surface formulation and computational mode-splitting, with barotropic and baroclinic time steps of 1 s and 30 s, respectively. A free-slip lateral momentum boundary condition is used, and the friction law at both the bathymetry and the ocean/atmosphere interface is assumed to be quadratic (non-linear) (Soontiens et al., 2016). A constant drag coefficient for the surface and bed of 2.5 x 10^{-3} is chosen (Soontiens & Allen, 2017).

The Monotonic Upstream-centred Scheme for Conservation Laws (MUSCL) scheme is used for tracer advection. The lateral diffusion scheme for tracers uses a rotated Laplacian operator acting along iso-neutral surfaces. The lateral diffusive velocity and length scales are set to 0.0009 ms^{-1} and 222 m, respectively (Okubo, 1971). The lateral diffusion scheme for momentum uses the bilaplacian operator acting in the horizontal (geopotential) direction with lateral viscous velocity and length scales of 0.3 m s^{-1} and 222 m, respectively. An energy and enstrophy conserving scheme and the Hollingsworth correction are applied (Hollingsworth et al., 1983; Penduff et al., 2007). The hydrostatic pressure gradient formulation is a Pressure Jacobian scheme, and the Generic Length Scale (GLS) scheme is used for the vertical turbulent mixing (Umlauf & Burchard, 2003).

2.2.2 Model bathymetry

The model bathymetry was derived from a bathymetric dataset compiled by Hogg et al. (2016) by averaging the 100 m resolution data onto the ~200 m grid (Fig. 1c). The main bathymetric features - including the deep channels, shallow banks, and the coastal topography - are mostly well captured at this resolution, with the exception that some small-scale features (such as sills) are smoother than observed.

Official bathymetric data for the seabed exposed following the recent retreat of Neumayer Glacier are not yet available. Shallow points in chart data and observed grounded icebergs suggest a shallow inner sill exists, also hypothesized by Hodgson et al. (2014) and referred to here as the 'postulated sill'. However, the width and depth of this potential sill are unknown. Therefore, in the baseline simulations, the choice was made to continue the known shallow gradient of the bed topography towards the glacier terminus along the center of the fjord, leading to a maximum depth of ~160 m adjacent to Neumayer Glacier. The adjacent data gaps were filled by creating a quadratic 'U' shape across the fjord, assuming shallow coastal points of 20 m depth. This allows for an unrestricted channel for the simulated water flow. To consider the impact of the postulated sill on the fjord oceanography, an artificial sill geometry was added for a process test simulation. This was achieved by modifying the bathymetry such that it shallowed steeply to 30 m across the width of the fjord, resulting in a bathymetric barrier one grid cell wide. East Bay has more thorough coverage of observational bathymetry data, including close to Nordenskjöld Glacier terminus, with a maximum depth of ~70 m adjacent to the glacier. A few individual grid cells were altered to allow a gentle shallowing towards the coastal edges of the fjord directly adjacent to the glacier and to give a smoother horizontal glacier terminus shape to aid model stability.

2.2.3 Open and surface boundary forcing

The model is forced at the open boundaries with tides from a global tidal model (TPXO9.2; Egbert & Erofeeva, 2002) using eight tidal constituents (Q1, O1, P1, K1, N2, M2, S2, K2) and with 3D flows, sea surface height, temperature, and salinity derived from a regional South Georgia model (Young et al., 2016). Forcing data from the regional model are bilinearly interpolated to the open boundary points. The barotropic open boundary forcing uses the Flather Radiation Scheme (Flather, 1994). The baroclinic flows are treated with the 'zerograd'

(Neumann) scheme, where the values at the boundary are duplicated with no gradient. Tracers at the boundary use the Flow Relaxation Scheme, which applies a simple relaxation of the model fields specified at the open boundary over a zone of 9 grid cells (Davies, 1976; Engedahl, 1995).

Surface boundary forcing is derived from the ERA5 reanalysis dataset with 30 km horizontal grid resolution (Hersbach et al., 2020). A bulk formulation (NCAR, Large & Yeager, 2004) is used. Interpolation of the coarse atmospheric forcing to the fine grid spacing of the model is achieved using the 'on-the-fly' option in NEMO4 and supplying a weights file for bilinear interpolation.

2.2.4 Terrestrial freshwater forcing

The freshwater contributions of surface run-off and subglacial outflow in the domain are taken from a theoretical climatological annual cycle calculated from historical precipitation data, glacier basin size, and positive degree days (Young et al., 2011). The freshwater flux for each glacier is injected into the appropriate ocean cell adjacent to the glacier and distributed over a prescribed depth range; the locations of glaciers contributing meltwater to the model are shown in Fig. 1c (red stars). For the two large marine-terminating glaciers in Cumberland Bay, the freshwater forcing required consideration of subglacial meltwater plume-driven dynamics. Based on knowledge from other high-latitude ice masses, it is assumed that a majority of surface meltwater from the glaciers descends through crevasses and moulins and enters subglacial channel systems at the bed (Chu, 2014). These channels meet the ocean at the grounding line of the marine-terminating glaciers at the fjord head, leading to the rise of subglacial discharge as a buoyant plume (Hewitt, 2020). The theoretical meltwater cycle is thus split into 10% surface runoff and 90% subglacial discharge. Given the uneven bathymetry, for the purposes of this modeling study, it was assumed that 'localized channels' are formed, which emerge at the deepest part of the glacier termini over a width of one grid cell (~200 m) (Slater et al., 2015). In practice, buoyant plumes tend to rise in contact with the submarine ice face, causing melt and continue to entrain ambient ocean water until they reach neutral buoyancy (or the surface), where they intrude horizontally into the ocean (Hewitt, 2020; Sciascia et al., 2013). As NEMO4 uses the hydrostatic assumption, it is not possible to resolve the plume dynamics within the model, and so a parameterization is required.

The default option for meltwater runoff in NEMO4 is to introduce fresh, cold meltwater into the surface layers of the model, extending down to a specified depth. However, this does not capture potentially important increased buoyancy-driven outflow and upwelling of deep waters as a result of subglacial discharge and could alter the ocean stratification unrealistically (Cottier et al., 2010). A new improvement has been developed for this study that adapts the freshwater input by incorporating the subglacial plume characteristics according to an offline plume model. This offline model requires ocean conditions, which necessitates an iterative process, as follows.

First, the model is run for ten years (following a year spin-up) with no terrestrial freshwater forcing. The deepest ocean grid cell column adjacent to the glacier is identified as the point to which the subglacial discharge would be directed via the hydraulic gradient. Next, an offline plume model is run that calculates the properties of the plume based on Slater et al. (2017; equations 4a – 4d) and the melt rate of the submarine ice face based on Jenkins (2011; equations 7 – 9). The plume model uses the temperature and salinity from the previously identified model grid cell column and the theoretical daily subglacial discharge, Q_S (Fig. 3a). Assuming values for the plume model constants following Slater et al., (2017), the model is solved for the temperature (T), salinity (S), volume per second (Q_P) and depth (D) at which the plume reaches neutral buoyancy (termination depth) (Fig. 3 b-e). Finally, the meltwater properties are set to the plume T and S and inserted into the relevant NEMO4 grid cell from the surface down to 10 m, or down to the termination depth, D, if the plume terminates (reaches neutral buoyancy) below the surface. It is not currently possible to simulate a wholly subsurface plume in NEMO4, though in the case when subsurface termination is predicted, a subsurface plume is ultimately achieved due to the higher density of plume water input compared to the near-surface ocean waters. The surface freshwater runoff (the remaining 10% of the theoretical daily meltwater) is inserted into an adjacent grid cell to that used for the plume model to simulate the portion that would remain on the glacier's surface running off from supraglacial streams. From here on, the meltwater-laced plume outflow is referred to as the WB-PLUME or the EB-PLUME for West Bay and East Bay, respectively, which consists of > 95 % seawater (Fig 3. a, d).

The new freshwater parameterization provides a representation of glacier plume and buoyancy-driven outflow within the limitations of the NEMO4 framework, which is not captured

293 by adding fresh, cold meltwater into the surface alone. Similar schemes have been implemented
294 previously in MITgcm and ROMS (Cowton et al., 2015; Oliver et al., 2020). However, though
295 the effect of entrainment into the horizontally spreading plume will be represented coarsely,

296 entrainment of ocean waters into the vertically rising plume is not included in this NEMO4
297 parameterization. Therefore, the ocean model does not capture the extent of a thick, but slow
298 inflow below the plume's neutral buoyancy (Cowton et al., 2015; Mortensen et al., 2011;

299 Sciascia et al., 2013). This limitation of the modeling approach is considered throughout and in
300 detail in section 4.

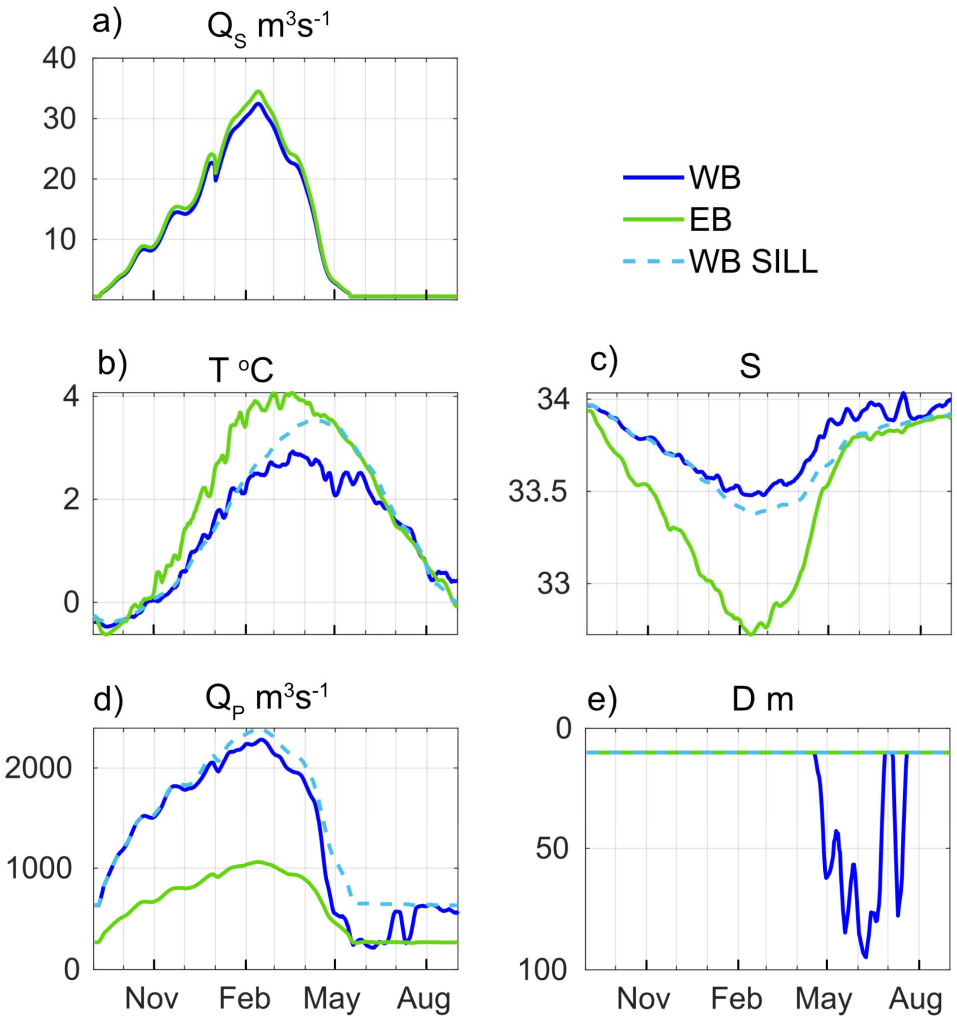

Figure 3. (a) The theoretical climatological cycle of meltwater discharge, Q_S, for Neumayer Glacier in WB (blue) and Nordenskjöld Glacier in EB (green) September 2005 to August 2006 (Young et al. 2011). (b) Conservative temperature, T, (c) absolute salinity, S, (d) volume per second, Q_P, and (e) neutral buoyancy (termination) depth, D, for WB-PLUME (blue) and EB-PLUME (green) in the baseline PLUME run and the for the WB-PLUME in the SILL-PLUME run (dashed blue) September 2005 to August 2006.

2.3 Model validation and run configurations

The model was validated using 11 months of CTD data collected in 2006 from the mouth of East Bay (Fig. 1b, pink star). The closest point to the mid-depth of each model level was taken from the observational data to allow direct quantitative comparison. The Root Mean Squared Error (RMSE) for conservative temperature and absolute salinity was calculated for each month of 2006 (excluding December when data were not collected), as well as the total RMSE (TRMSE). The mean near-surface error (MSE) (average of each point in the top 10 m) and mean near-bed error (MBE) (bottom model level) were calculated by subtracting observational data from model data. Finally, the Cost Function (CF) was calculated, which is a measure of model predictive skill that incorporates the standard deviation of the observational data (Holt et al., 2005). The results (Table 1) suggest that the model reproduces the observed temperature very well, with the CF value well below 1 at this location. Although the CF for salinity is over 1, likely due to the timing of freshwater input (see section 3.1.1), the TRMSE is relatively small, demonstrating that this model is a useful tool for exploring the drivers of spatial and temporal variability.

	TRMSE	**MSE**	**MBE**	**CF**
T	0.39 ^{o}C	-0.04 ^{o}C	-0.24 ^{o}C	0.09
S	0.19 g kg^{-1}	-0.02 g kg^{-1}	0.01 g kg^{-1}	1.19

Table 1. Results of statistical tests from model validation.

The model is initially run from 1999-2000 to allow spin-up from initial conditions interpolated from an existing regional model (Young et al., 2016). Then the full model is run for 2000 – 2012 without the postulated sill. Process tests, which test the sensitivity of the system to individual factors, are run for September 2005 to August 2006. The baseline scenario is referred to as PLUME, and the test removing WB-PLUME and EB-PLUME is referred to as NOPLUME. Inserting the shallow sill in WB and recalculating WB-PLUME and EB-PLUME via the same method as the baseline is referred to as SILL-PLUME. Inserting the sill without the WB-PLUME and EB-PLUME is referred to as SILL-NOPLUME.

3 Results

3.1 Seasonal and spatial variability

3.1.1 Temperature and salinity

The time series from the point source CTD data in 2006 reveals a strong seasonal cycle in conservative temperature (T) and absolute salinity (S) (Fig. 4). The water column is stratified in austral summer and early autumn, with the warmest surface waters between February and April due to surface heating, reaching a maximum of 4.1 ^{o}C in March, and with temperatures decreasing with depth. The water column cools in autumn and winter to a minimum of 0 ^{o}C by surface cooling, and the water column is well mixed between August and October (Fig. 4a) due to mixing from winter storms. A fresh near-surface lens is observed between March and July, with a minimum salinity near-surface of 32.9 in April. This is likely a combination of precipitation and the melting of floating ice since this point is a significant distance from the glaciers. Salinity increases with depth, with the greatest salinity of 34.3 near-bed between January and June, characteristic of inflowing dense shelf waters. Modeled temperature and salinity for the same location and year are largely consistent with the CTD data (Fig. 4b). The most significant difference in temperature is that the model predicts temperatures below zero (Fig. 4b). The timing of the seasonal salinity cycle is less consistent with the CTD data, with the fresh surface layer predicted ~2 months earlier than observed. This may be because the theoretical melt cycle does not consider a time delay between surface heating and coastal fluxes of freshwater. In addition, as it is a climatology, the meltwater cycle is not calculated on atmospheric conditions specific to 2006.

The CTD transect data from WB and EB provide some spatial context for the seasonal cycle. Hereafter, the seasonal cycle is described from spring (September) through to winter (August), and the transect CTD data from 2012, 2020, and 2021 are ordered according to season rather than year (Fig. 5). For each survey, the transect plots start from the CTD cast closest to Neumayer Glacier in West Bay and end close to Nordenskjöld Glacier in East Bay (Fig. 1b dashed grey line), with distance along the transect referenced to the central point between WB and EB mouths. In November (late spring), the warmest surface waters are at the fjord mouths and close to Neumayer Glacier (Fig. 5a). Near-bed waters slightly increase in temperature near

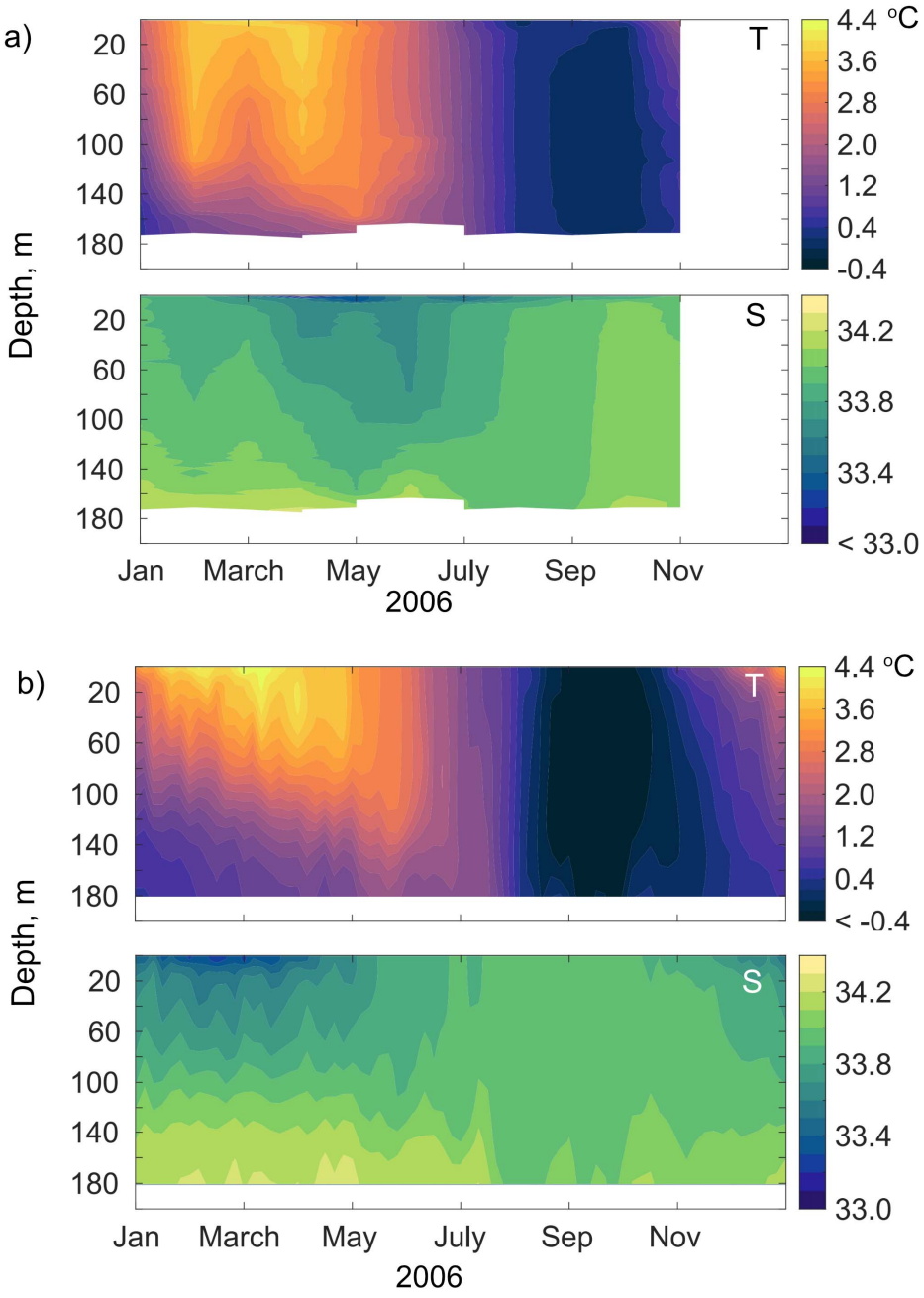

Figure 4. Conservative temperature (T) and absolute salinity (S) from (a) the CTD survey taken in the mouth of East Bay (Figure 1b, pink star) for each month, excluding December, in 2006, and (b) from the equivalent model location for each 5-day mean January to December 2006.

355 the mouth of EB. A thin near-surface fresh lens extends along the length of WB and near
356 Nordenskjöld Glacier in EB. In February (late summer), there is a cold surface layer close to
357 both Neumayer Glacier and Nordenskjöld Glacier, notably colder in WB. Near-bed temperatures
358 are slightly higher across the fjord mouths. The fresh surface lens observed in spring is again
359 evident in summer, though fresher and deeper. In April (autumn), the upper ~100 m is more
360 mixed and cooler. A thin, fresh surface lens is again apparent, weaker than summer and more
361 constrained spatially to WB mouth and mid-way along EB.

362 The transects indicate that glacier processes may modify the water properties at the head
363 of each fjord arm through cooling and freshening, particularly in summer. Near the fjord mouth,
364 shelf-fjord exchange processes increase salinity at depth and in spring and summer, result in a
365 near-bed intrusion of slightly warmer water. In February, the water mass properties below 25 m
366 are very similar along the entire transect, but surface waters are notably colder and fresher in WB
367 (Fig. 5). The Temperature-Salinity (T-S) lines for WB (Fig. 6a, purple lines) show the signature
368 of melted glacial ice mixing with seawater; shallower than 50 m, the lines approximately follow
369 a melt line (grey line Fig. 6a), which has a slope of roughly 2.5 ^{o}C per salinity unit (Gade slope,
370 Gade, 1979; Mortensen et al., 2013; Straneo & Cenedese, 2015). This signature of melt could be
371 both due to the direct melting of the submarine ice face and the submarine melting of icebergs.
372 The change in the slope of the T-S lines closer to the surface suggests that these waters are
373 modified by a mixture of submarine melt, subglacial discharge, and surface melt as they lie
374 between the melt and runoff lines (Straneo & Cenedese, 2015).

375 The along-fjord WB transect T-S diagram for the November observations (Fig. 6a) shows
376 the upper water column (< 50 m) does not have signals of submarine melt. However, the slope of
377 the T-S line in the near-surface waters in the vicinity of the postulated inner sill (Fig. 6a, green
378 dot-dash lines) suggests the influence of surface runoff. This runoff may be from the surface
379 melting of a nearby grounded iceberg (observed by the author) or the land-terminating Lyell
380 Glacier on the south coast of WB. The dip around 50 m in November may be remnant winter
381 water below the surface warmer water layer. As the November CTD casts in WB and EB were
382 almost one week apart, short-term changes in atmospheric conditions may explain the near-
383 surface differences between WB and EB. The data in the vicinity of the postulated sill in
384 November do not extend all the way to the bed. As the full water column may not have been

captured, this limits the comparison between the inner and outer basin and, thus, limits understanding of the influence of the inner sill on oceanographic variability.

Along EB, the near-surface waters closely follow the runoff line in April and somewhat in November (Fig. 6), most likely the influence of Nordenskjöld Glacier, to which the surveys were significantly closer than the WB surveys were to Neumayer Glacier (Fig. 1b). Near-bed, the T-S lines for November show the intrusion of the slightly warmer, higher salinity shelf waters in EB but not in WB, suggesting different exchange mechanisms at the mouth of each arm. There are clear differences seen between WB and EB in the near-surface and near-bed waters in both spring and summer, suggesting underlying physical drivers of oceanographic variability impact each fjord arm in different ways.

As the spring, summer, and autumn surveys were not conducted in the same year, it is possible that some of the spatial and seasonal variability is being conflated with interannual variability. The only available data for examining interannual variability are point data from the mouth of EB between 2004 and 2006 for February, June, and October (Fig. 7). Whilst weaker than the seasonal variability, there is significant interannual variability in T and S, most notably in austral summer and early winter, with maximum near-surface T differences of ~2 ^{o}C in June (Fig. 7a), and maximum S differences of ~1.2 g kg^{-1} in February (Fig. 7b). Interannual variability in surface heating may be a key driver of the observed variability, directly impacting water column temperatures but also driving variability in local glacier melt and, thus, salinities within Cumberland Bay. The high interannual variability in June is not seen by October, which suggests a high flushing rate of in-fjord waters in autumn and winter, with the less variable shelf waters important for establishing water properties in Cumberland Bay by spring.

The hydrographic data reveal some spatial differences between WB and EB. However, the CTD surveys do not extend close enough to Neumayer Glacier terminus to detect important differences in the glacier adjacent water column properties, and there are no data on the ocean currents. Further investigation requires analysis of the regional high-resolution ocean model.

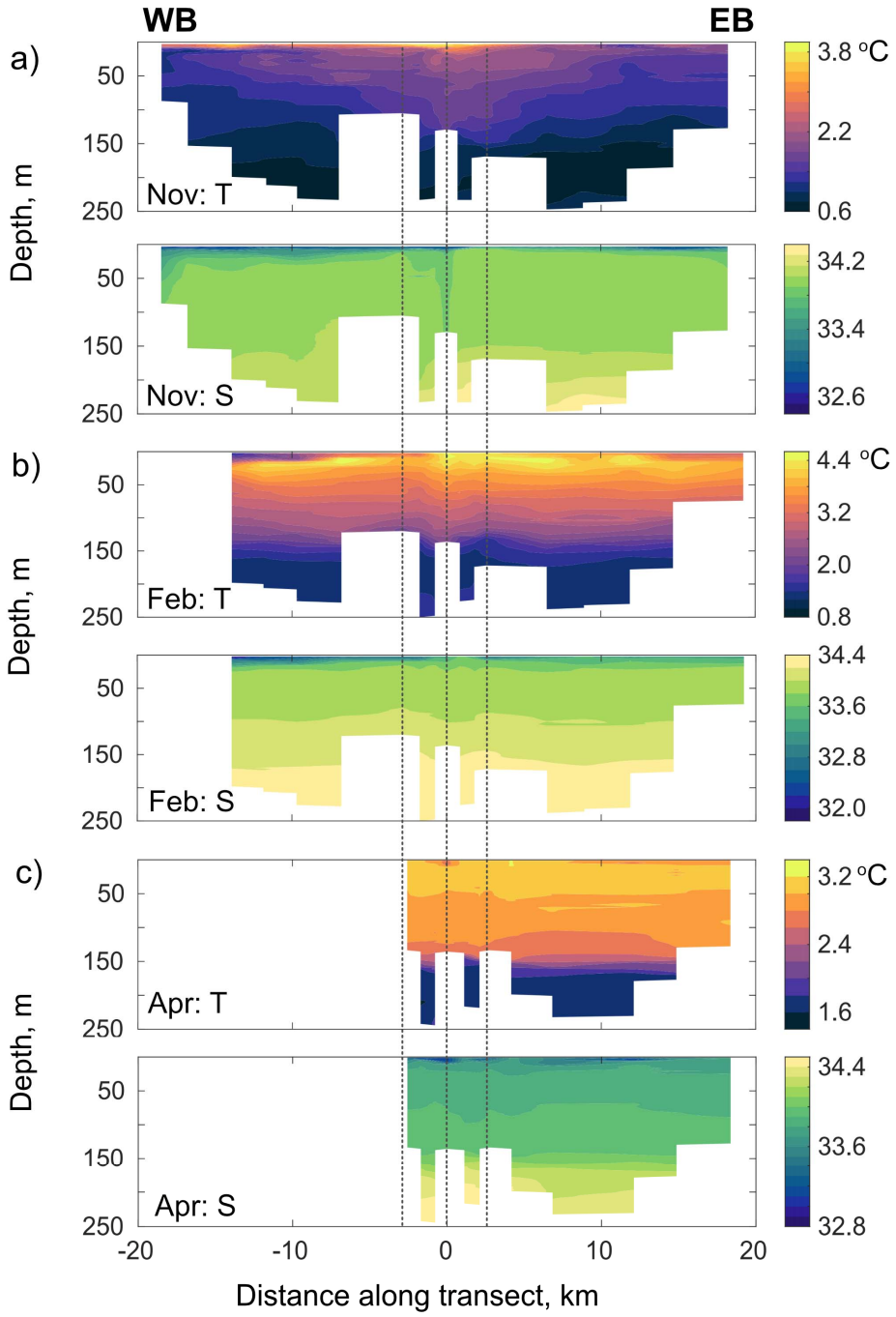

Figure 5. Transects (WB to EB; grey dashed line in Fig. 1b) of conservative temperature (T) and absolute salinity (S) for CTD surveys from (a) November 2021, (b) February 2020 and (c) April 2012. Black dashed lines indicate where the cross-mouth transects start and end. Note, the color bar scales are different for each month.

411

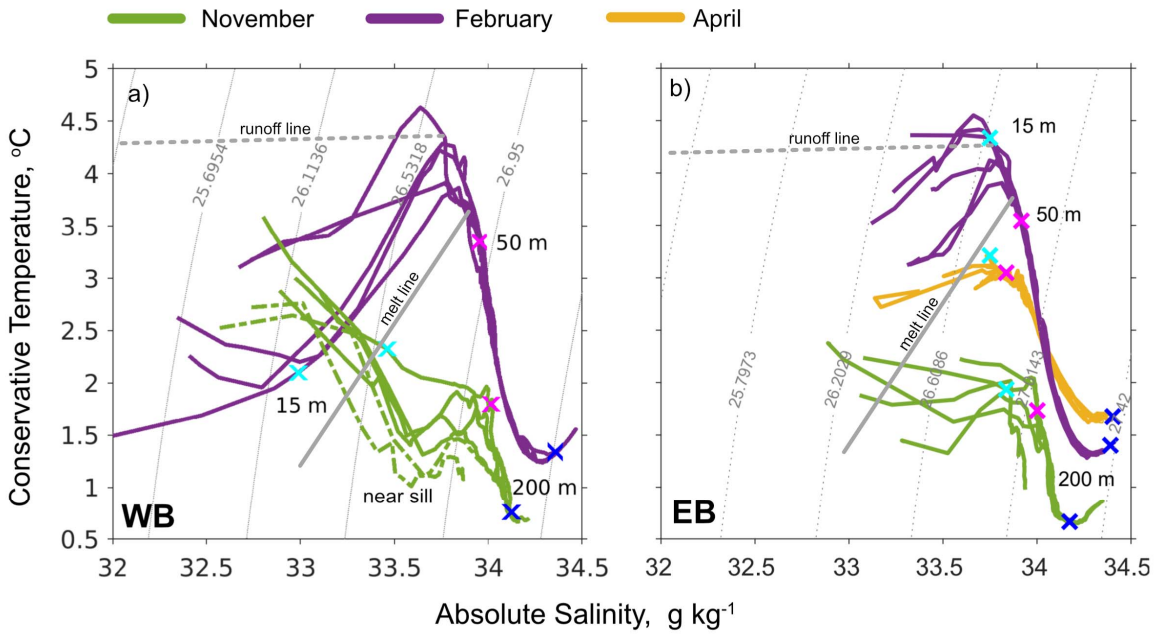

Figure 6. Temperature-Salinity (T-S) diagrams for all CTD casts taken along the length of a) WB and b) EB in April 2012 (yellow), February 2020 (purple) and November 2021 (green). Dashed green lines indicate where the CTD cast was in the vicinity of the postulated inner sill. The melt line (grey solid line) and runoff line (grey dashed) are overlaid, and density contours (kg m^{-3} - 1000) are in the background. Depths 15m (cyan), 50 m (pink) and 200 m (blue) are marked with crosses.

412

413

414

415

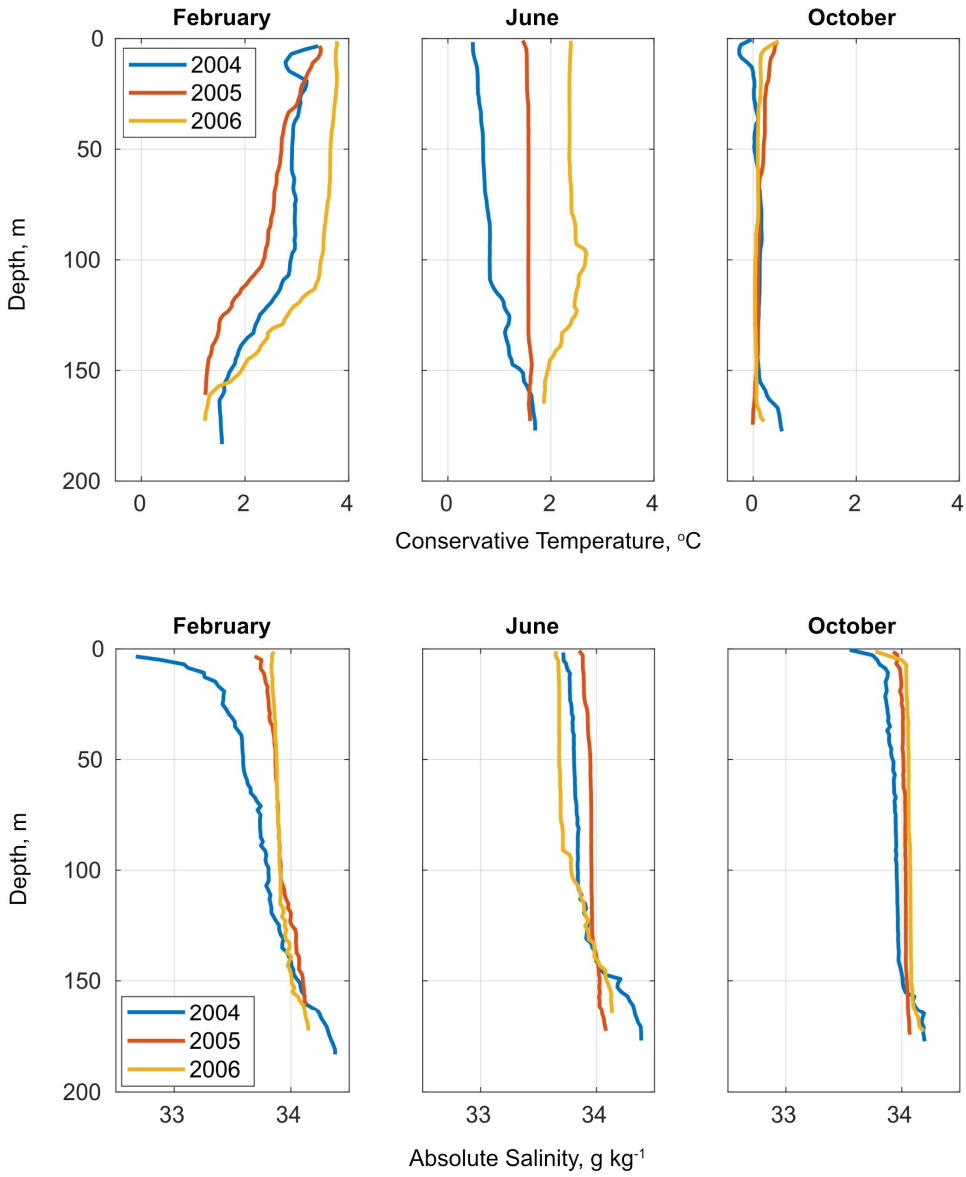

Figure 7. a) Conservative temperatures and b) absolute salinity from the mouth of EB (Fig. 1 b, pink star) in February, June and October for 2004, 2005, and 2006.

416

417

418

3.1.2 Flow fields and sea surface temperature

A more detailed description of spatial and temporal oceanographic variability in Cumberland Bay can be gained from analysis of high-resolution model output, here focusing on near-surface flows, mid-depth (100 m) flows and sea surface temperatures (SST) (Fig. 8). The seasonal variability is illustrated with monthly averages for November (spring), February (summer), May (autumn), and August (winter).

In spring and summer, there is enhanced surface (top model layer) outflow along the north coast of WB and the east coast of EB, which crosses to the west coast at the mouth, and is subsequently entrained into the stronger northwestward shelf flows (Fig. 8a). The Rossby radius of deformation is larger than the narrow fjord width, so cross-fjord variations are not induced by the Coriolis force (Cottier et al., 2010). The baroclinic surface flows are strongest in summer when the volume of meltwater runoff, and therefore buoyancy-driven outflow, is greatest (Fig. 3a). At 100 m, flows are much weaker with strong cross-fjord variability and eddy-like features at the fjord mouths (Fig. 8b), although the model representation of flows at depth may be impacted by the lack of plume entrainment and subsequent deep inflow in the model, discussed further in section 4.3. Surface flows weaken in autumn, as meltwater runoff reduces steeply (Fig. 3a). There is a strengthening of recirculation at 100 m in both bays in autumn, extending the length of each arm (Fig. 8b). Winter storms drive mixing which weakens the stratification allowing bathymetric steering of coastal flows into the fjord mouth. The buoyancy-driven outflow is no longer the dominant driver of circulation in winter, reflecting the seasonality of freshwater forcing.

The sea surface temperature (SST) is cold in spring (~0 ^{o}C), coldest in the tributary fjords and at the head of WB (Fig. 8c). The SST warms significantly in summer and autumn (~3-4 ^{o}C) though notably colder in WB compared to EB. The colder surface waters in WB are consistent with the colder properties of WB-PLUME compared to EB-PLUME (Fig. 3b). In winter, the SST is similar between the fjord arms, consistent with the lower volume of the WB- and EB-PLUME and buoyancy-driven outflow no longer being a dominant driver of circulation.

While many aspects of seasonal variability are not yet verified, the model provides a useful tool for testing hypotheses. Variability in shelf-fjord exchange, apparent in the flow fields and near-bed water properties, and the interaction of such flows with the fjord outer sills, will

449 contribute to temporal and spatial variability at the fjord mouths. However, this is beyond the
450 scope of the present study. Instead, based on the clear influence of glacial meltwater in the data,
451 we focus on the role of buoyancy-driven outflow in driving spatial and temporal variability in
452 Cumberland Bay.

453

454

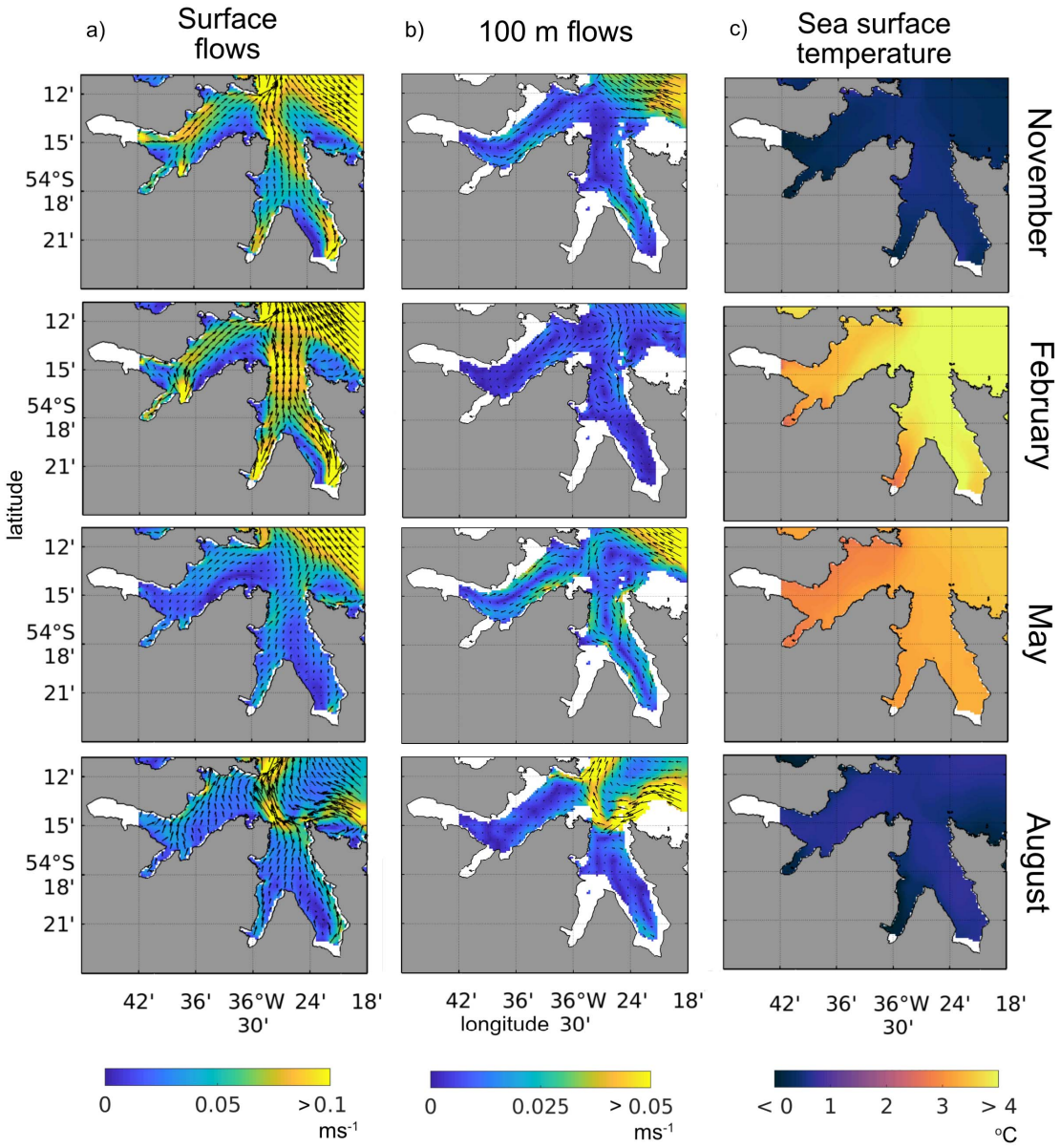

Figure 8. Surface flows, 100 m flows, and sea surface temperature, averaged over the months of November, February, May, and August. Note the difference in color scale between the surface and 100 m flows.

455

456

457 ### 3.2 Drivers of variability

458 #### 3.2.1 Buoyancy-driven outflow

459 To understand the influence of buoyancy-driven outflow on seasonal and spatial
460 variability, we examine the volume transport through cross-sections near to Neumayer and
461 Nordenskjöld Glaciers. We consider the near-glacier zone to be within ~1 km, or 5 grid cells,
462 from the modeled termini positions, which allows for the oceanography to adjust to the
463 parameterized plume input. We find a distinct difference in circulation patterns in this zone
464 between the two fjord arms (Fig. 9, locations of cross-sections in Fig. 1c, red dashes). In WB, the
465 average volume transport in November shows a 4-layer structure from the surface to the bed of
466 alternating outflow and inflow. In February, when the volume of WB-PLUME is greatest (Fig.
467 3d), there is strong outflow in the north, with weaker inflow in the south in the upper ~60 m. The
468 outflow in the north becomes a subsurface feature in May with surface inflow across the width of
469 WB; this coincides with a sharp reduction in WB-PLUME volume and the onset of subsurface
470 WB-PLUME termination (Fig. 3e). In August, following a period of low WB-PLUME volume,
471 the structure reduces to 2-layers.

472 In November in EB, there is a predominant 2-layer structure of surface inflow and
473 outflow at depth in the west, with the reverse structure in the east (Fig. 9). This pattern continues
474 largely unchanged in February and May, before a distinct shift in August to inflow in the west
475 and outflow in the east (Fig. 9), due to more barotropic flows in the destratified winter water
476 column (Fig. 4). The EB-PLUME is confined to the upper 20 m, increasing the strength of the
477 surface outflow in spring and summer in line with the near-surface flows (Fig. 8). To test the
478 exact influence of the WB- and EB-PLUME on the circulation patterns, we compare directly to
479 the NOPLUME scenario. The total volume transport through each section was integrated across
480 the fjord width and averaged over 30-day intervals to enable visualization of the seasonal cycle
481 in transport variability with and without the PLUME (Fig. 10). In WB, the thick surface outflow
482 that moves subsurface between April and July is clearly a response to the WB-PLUME; with
483 NOPLUME, there is a thin surface outflow and subsurface inflow between ~10 and 50 m
484 throughout the year (Fig. 10a). In EB, outflow is confined to the upper ~20 m for the majority of
485 the year with EB-PLUME, becoming thicker and weaker in winter. With NOPLUME the
486 transport pattern remains the same but with weaker surface outflow (Fig. 10b). Should the inflow

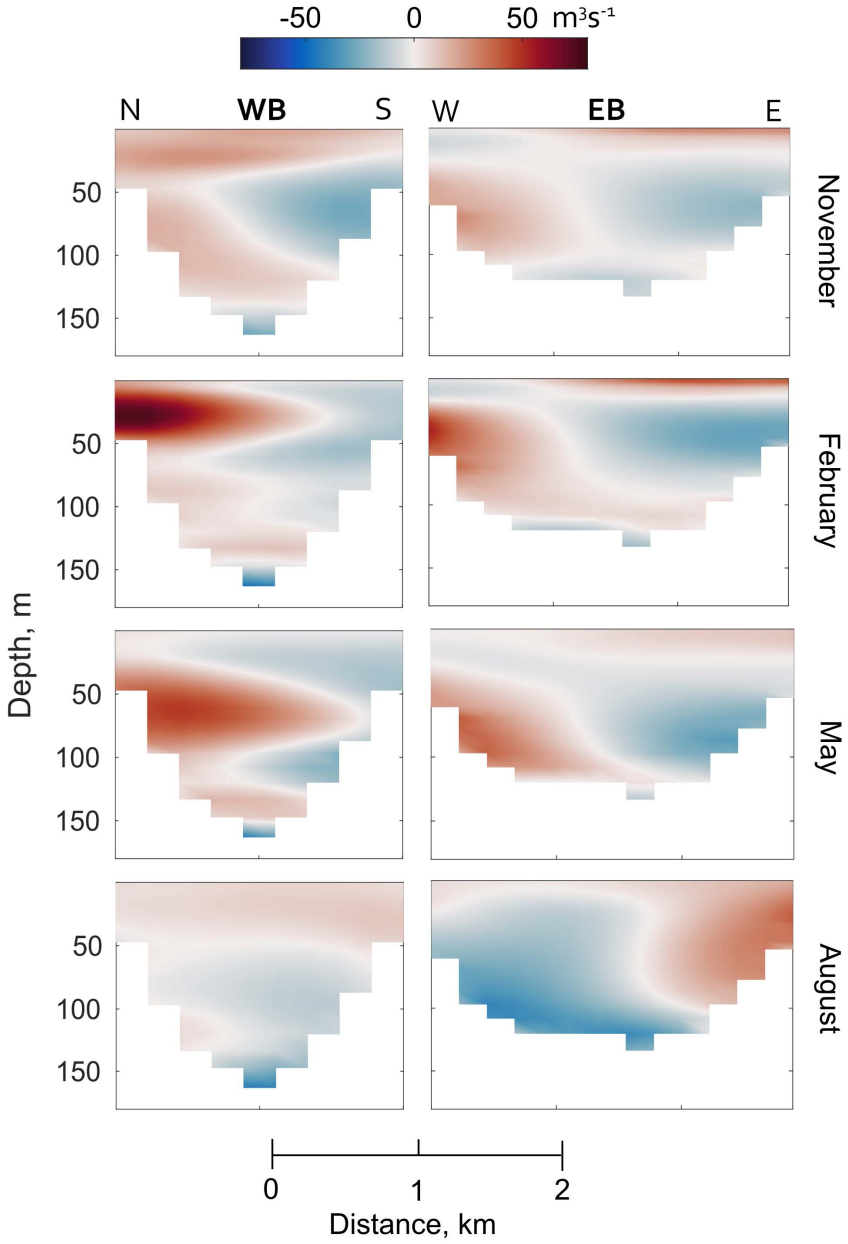

Figure 9. Monthly-averaged volume transport through cross-sections ~1 km from Neumayer Glacier (WB, north (N) to south (S)) and Nordenskjöld Glacier (EB, west (W) to east (E)) (Fig. 1c, red dashed lines). Red indicates outflow, toward the fjord mouth, and blue indicates inflow, toward the glaciers.

487 induced by the vertical plume entrainment be represented, we would also expect to see a greater
488 increase in net inflow (or decrease in net outflow) below the plume outflow in both WB and EB.

489

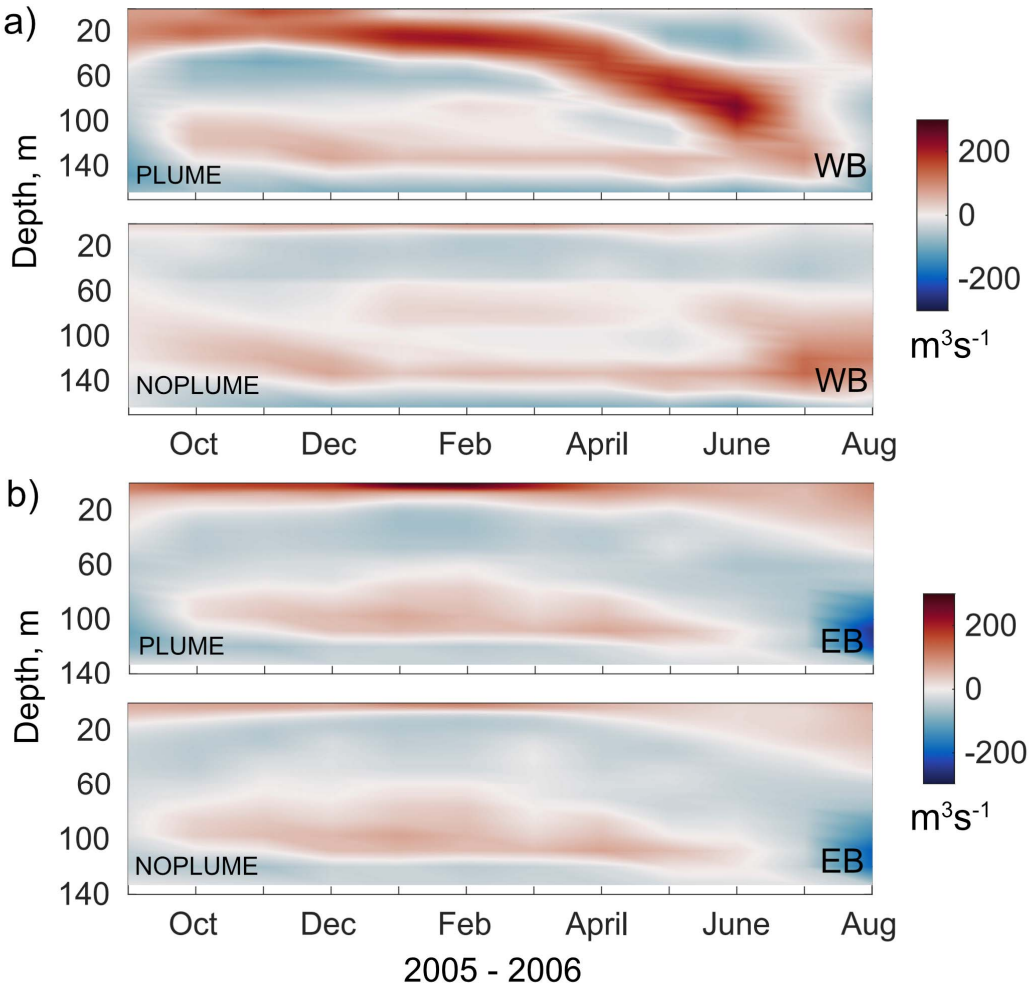

Figure 10. Monthly-averaged volume transport integrated across model levels through cross-sections ~1 km from (a) Neumayer Glacier (WB) and (b) Nordenskjold Glacier (EB) (red dashed lines in Fig. 1c), comparing PLUME and NOPLUME model runs; September 2005 to August 2006.

Though the volume transports discussed above lack the plume entrainment-driven inflow, we do believe these plots show sensible results in this near-glacier zone. We expect to see a seasonal plume-driven (sub)surface outflow and a consistent deep inflow year-round. The mid-depth inflow and outflow are assumed to be largely driven by the propagation of intermediary exchange at the fjord mouth due to density differences between the shelf and in-fjord waters (investigation of which will be the focus of future work). The T and S in this near-glacier zone also yield sensible results (not shown), with a similar stratification and seasonal variability as found for EB mouth (Fig. 4). Notably, however, the upper water column near-glacier in WB is colder and more saline than in EB, which we expect to see due to the upwelling via a deeper subglacial plume.

A key difference between WB and EB is the seabed depth adjacent to the glaciers. WB is deeper; hence, the water properties used to calculate WB-PLUME are colder and more saline relative to those in EB (Fig. 3), and this is reflected in the SST (Fig. 8). The outflow of WB-PLUME is greater and spread over a larger depth in WB compared to EB. Due to the volume of subglacial discharge and the properties of the water in autumn, the plume in WB terminates below the surface, driving a different circulation pattern at this time of year (Fig. 9). These results strongly suggest the subglacial plume drives an important mode of circulation, and the plume dynamics are sensitive to the relatively small depth range of these shallow glaciers. Given the spatial disparity between WB and EB driven by the plume, it is possible that the retreat rates of Neumayer and Nordenskjöld Glacier are sensitive to the small differences in oceanography, discussed further in section 4.2. However, a perhaps more significant driver of spatial differences in oceanography is the postulated inner sill in WB.

3.2.2 West Bay postulated inner sill

The model simulation was repeated with an inner sill artificially inserted in WB as a barrier 1-grid cell wide and sitting at 30 m below the sea surface (Fig. 11a, location in Fig. 1c, white dashed line) (SILL-PLUME). Analysis of water properties in April for a transect along the center of WB shows the new inner basin to be warmer, fresher, and well-mixed compared to the outer basin (Fig. 11a). The near-bed temperature in the center of the inner basin is ~2 ^{o}C higher than the comparable PLUME run (Fig. 11b). Higher near-bed temperatures are also predicted by the SILL-NOPLUME simulation (Fig. 11b), which shows that the inner sill is the underlying

driver in both cases. Warmer, fresher surface waters from the outer basin flow over the sill, where they are mixed, while deeper waters are blocked by the sill, leading to near uniform T and S in the inner basin (Fig. 11a), similar to observed processes over transverse ridges on the West Antarctic Peninsula shelf (Venables et al., 2017). With no sill present, WB-PLUME decreases the near-surface temperature in summer and autumn (Fig. 11b, blue lines). For the SILL-PLUME scenario, WB-PLUME decreases the near-surface temperature in summer and slightly increases the near-surface temperature in autumn (Fig. 11b, red lines). Therefore, the presence of the sill affects the full water column in the inner basin, but the most significant changes are near-bed with the increase in temperature, which may have implications for glacier retreat.

The integrated volume transport through the WB section was calculated for the SILL-PLUME and SILL-NOPLUME simulations for comparison with the results described in section 3.3. The transport patterns through the section, which now lies within the inner basin, show that when a sill is present, the buoyancy-driven outflow drives a different circulation pattern (Fig. 12). The SILL-PLUME simulation predicts a thick surface outflow throughout the year in the upper ~50 m, deepening in winter, and inflow between ~50 and 100 m from spring to early autumn. Below ~100 m, there is relatively low volume transport in spring and summer and a strong inflow in autumn and winter. Compared with the SILL-NOPLUME run, it is apparent that the WB-PLUME is driving the pattern of strong outflow overlying inflow in spring and summer and extending the duration of near-bed inflow in autumn and winter. As the peak of the sill is 30 m below the sea surface, a portion of the buoyancy-driven outflow flows over the sill, but below 30 m, the outflow is blocked by the sill and re-circulates as subsurface inflow, the strength and depth of which would likely be increased with the inclusion of plume entrainment-driven inflow. Warmer surface waters from the outer basin flow into the inner basin over the sill along the south coast in the spring and summer (not shown), but integrating the volume transport along model levels masks this cross-fjord variability as the outflow from the plume dominates. In winter, as the volume of the WB-PLUME lessens and the density in the outer basin increases (temperatures cool and salinity increases, Fig. 4), waters from the outer basin encroach into the inner basin, sink, and present as a strong inflow at depth (Fig. 12).

An important difference between the model runs with and without an inner sill is that the PLUME run no longer has a sub-surface terminating plume for a portion of the year in WB (Fig. 3e). Due to the now uniform density within the inner basin resulting from the sill, the plume,

551 derived from SILL-NOPLUME, does not reach any neutral buoyancy before the surface at any
552 time of the year.

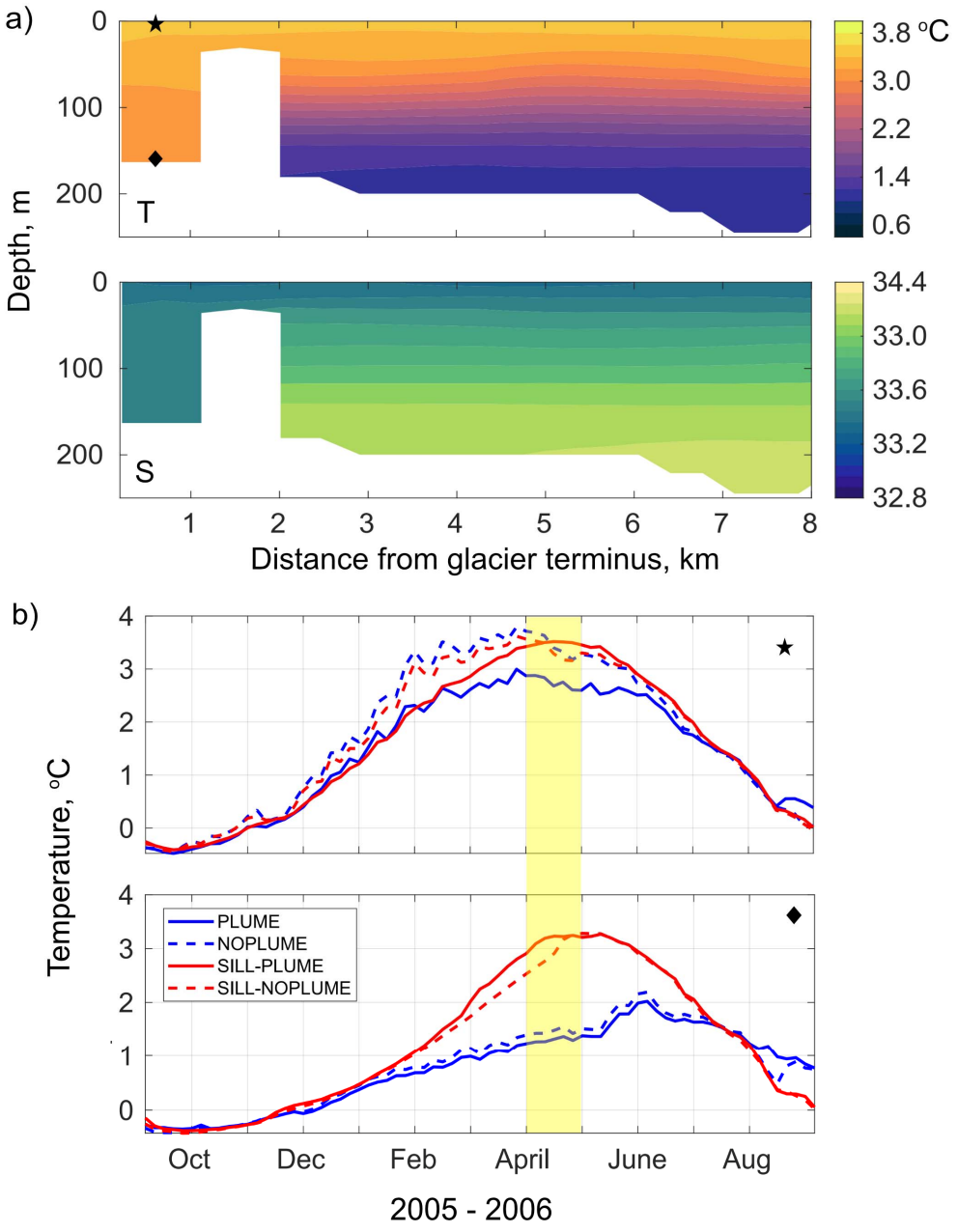

Figure 11. (a) Monthly averaged (April 2006) conservative temperature (T) and absolute salinity (S) from the SILL-PLUME model run for an 8 km transect along the centre of WB from Neumayer Glacier terminus. (b) 5-day mean near-surface (star in panel (a)) and near-bed (diamond in panel (a)) temperatures for September 2005 to August 2006, from the four model runs defined in the legend. The month of April is highlighted in yellow.

553

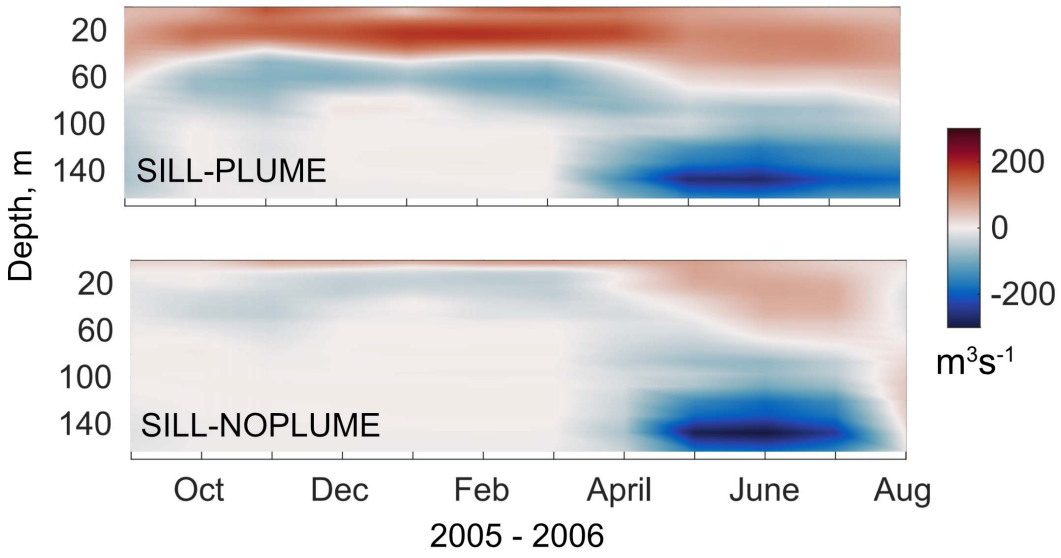

Figure 12. Monthly averaged volume transport integrated across model levels though the cross-section in WB (red dashed line Fig. 1c) for the SILL-PLUME and SILL-NOPLUME model runs; September 2005 to August 2006 Red indicates transport toward the fjord mouth, and blue indicates transport toward the Neumayer Glacier terminus.

4 Discussion

4.1 Oceanographic variability and limitations

The oceanographic data presented and analyzed in this study provide valuable information on the hydrography of Cumberland Bay. Freshwater signals are apparent in the data, but whether this can be attributed to surface meltwater runoff, subglacial discharge, melting of ice mélange, or increased precipitation is not completely clear. The cold, fresh signature of meltwater emerging as subglacial discharge may not be retained due to plume entrainment, meaning this can be hard to identify in the CTD data (Carroll et al., 2015). The oceanographic data reveal a strong seasonal cycle likely due to the combined effects of freshwater forcing, shelf-fjord exchange, and atmospheric forcing (particularly winds). However, the temporal and spatial limitations of the observational data hinder a more detailed analysis.

With the use of the new high-resolution oceanographic model, we identified that freshwater forcing, which is assumed to be dominated by subglacial discharge at the two main glaciers at the heads of WB and EB, is a key driver of spatial variability in the upper water column in spring through to autumn. This is due to the seasonal cycle of subglacial meltwater input and the bathymetric differences between the fjord arms. Wind forcing and fjord-shelf exchange likely dominate the spatial variability in flows in winter and are the focus of ongoing research.

The addition of the postulated inner sill in WB has a significant impact on the simulated seasonal and spatial variability and has implications for the retreat of Neumayer Glacier, discussed further in section 4.2. Neither scenario can yet be considered a more accurate representation of WB as the true bathymetry and the extent of the sill are unknown. However, the results clearly identify the sensitivity of the fjord oceanography to bathymetry and geometric controls on the circulation regime and suggest that buoyancy-driven circulation is likely to have varied considerably at different stages of past glacier front positions.

Though the model provides useful insights, the caveats must be considered. It is stressed that the plume dynamics and ocean model are not coupled, and the meltwater cycle is a climatology, which limits the interpretation of the results. The ambient water column entrained in the offline plume model is unmodified by freshwater forcing, and the circulation resulting from entrainment into the plume is not captured, suggesting the ocean model may be underrepresenting the net toward glacier flow at depth. The influence of plume entrainment-driven inflow is likely to affect the results of this study, discussed in detail in section 4.3. Additionally, the melting of icebergs is not represented in the model but is likely to have some influence on the hydrography and circulation (Davison et al., 2020). Despite these limitations, this study provides valuable insights into the oceanographic variability in Cumberland Bay while emphasizing the importance of representing plume dynamics for the simulation of circulation in fjords with marine-terminating glaciers.

4.2 Implications for glacier retreat

Neumayer Glacier in WB has retreated far quicker than Nordenskjöld Glacier in EB over the past century but the drivers of this differential retreat rate are currently unknown. We find that buoyancy-driven outflow arising from the subglacial plume parameterization has a markedly

different influence between bays. However, when the postulated inner sill is not present, the subglacial plume parameterization drives a greater degree of cooling in WB due to the upwelling of deeper, colder waters. Additionally, the subsurface termination of WB-PLUME is likely to weaken the strength of the overturning circulation, which has been linked to the strength of horizontal circulation, which in turn drives front-wide glacial melting (Zhao et al, 2022). Therefore, plume dynamics alone do not provide a persuasive argument for the observed differential glacier retreat. We hypothesize here that changes to water column properties adjacent to Neumayer Glacier due to the postulated shallow inner sill in WB are playing a key role in the differential retreat rate, alongside an ice-dynamic response following a retreat from a pinning point.

The results of model experiments show that the presence of a bathymetric barrier representing the postulated inner sill blocks colder waters at depth, resulting in a warmer, well-mixed inner basin (Fig. 11a). This warmer water in the vicinity of the glacier terminus can be inferred to increase glacier melt, and even potentially drive a positive feedback mechanism that would further increase glacial retreat from the sill, although as there is no ice-plume-ocean coupling in the model, such implications remain speculative. The melt rates directly at the terminus of Neumayer Glacier cannot be sensibly calculated due to the parameterized plume representation and lack of entrainment-driven inflow, but we can reasonably infer that melt rates are likely to be higher for SILL-PLUME than PLUME due to the warmer waters (increased thermal driving) in the inner basin. Therefore, the observed rapid retreat of Neumayer Glacier may be the consequence of a positive feedback mechanism, whereby warmer water is trapped and recirculated in the inner basin, promoting higher submarine melt rates through increased thermal driving and potentially increased horizontal velocities. Increased submarine melting will increase turbulence and reduce the density of the inner basin, driving a stronger inflow of warmer waters, thus promoting further melting. Additionally, warmer waters at depth may promote undercutting, which could lead to greater mass loss through calving (Benn et al., 2017). This, together with over-deepening bed topography beyond the postulated inner sill, provides a persuasive mechanism for the observed rapid retreat of Neumayer Glacier, where the potential intensification of ocean melting may have prevented Neumayer Glacier terminus from re-stabilizing. The processes described here, and the proposed positive feedback mechanism, are not present in EB as the inner sill peak is much deeper.

It remains unclear what caused Neumayer Glacier to retreat from the postulated inner sill in the first instance. Further exploration of this hypothesis requires a more comprehensive study, including detailed bathymetric surveys of the head of WB up to Neumayer Glacier terminus and a more accurate model representation of the WB inner sill. Future modeling work could be greatly enhanced by developing an ice-ocean-atmosphere coupled model at higher spatial resolution.

In previous studies focused on Greenland fjords, the presence of a shallow sill has been shown to reduce the melting of tidewater glaciers due to colder waters overlaying warmer waters (Millan et al., 2018; Schaffer et al., 2020). We find that in fjord systems where warmer waters overlay colder waters, the opposite holds, and a shallow sill may promote higher melt rates.

4.3 Influence of plume entrainment-driven inflow

As previously noted, it is not currently possible to resolve subglacial plume dynamics in the NEMO4 framework. The parameterization developed for use in this study captures the upwelling effect of a buoyant plume and the strong buoyancy-driven outflow where the plume reaches neutral buoyancy. The effect of plume-entrainment-driven inflow into a vertically rising plume has been neglected, however. We discuss here the likely influence of such inflow on the results of this study.

Turbulent entrainment of ambient waters into the subglacial discharge plumes has previously been modeled to drive a deep, thick, but weak inflow below the depth of neutral buoyancy (Carroll et al., 2015; Cowton et al., 2015; Sciascia et al., 2013). In a typical Greenlandic fjord setting, this compensating inflow has been shown to act as a mechanism for transporting warm, deep Atlantic waters in-fjord in summer and serves to restore salinity distribution in the fjord as runoff decreases into winter (Cowton et al., 2015; Sciascia et al., 2013). The strength and depth of the entrainment-driven inflow are dependent on the geometry of the subglacial conduit and submarine ice face, as well as fjord stratification (Carroll et al., 2015; Jackson et al., 2017). In idealized fjord studies, this deep inflow has been shown to be significant for providing heat for glacial melt (Cowton et al., 2015, 2016; Sciascia et al., 2013) and can potentially drive a deep melt-circulation feedback aiding the spin-up of standing eddies (Zhao et al., 2023). However, observational studies of Greenlandic fjords suggest net transport within the fjord is controlled by complex interactions between different modes of circulation

driven by a combination of forcings, such as the winds and tides. As such, subglacial plume-driven entrainment is not necessarily dominant when interacting with fjord-shelf exchange (Mortensen et al., 2014; Straneo et al., 2011).

In the present study, in the absence of the WB inner sill, we find that the differing plume dynamics between the two fjord arms do not provide a convincing argument for the rapid retreat of Neumayer Glacier in WB, compared to Nordenskjöld Glacier in EB. Should plume entrainment-driven inflow be included in this case, it is likely to act as a mechanism for increased transport of deeper shelf waters in-fjord (Cowton et al., 2016), thus generally reducing the temperatures and increasing salinity. Therefore, we would expect to find a greater reduction in temperature in WB than EB, due to the larger volume of entrained seawater (Fig. 3d), supporting the argument that plume dynamics alone are not the driver of differential glacier retreat.

Now, considering the case with the postulated inner sill, we find that this does provide an argument for differential glacier retreat due to the trapping of warmer waters inside the inner basin. If plume entrainment were to be included in this case, it may result in a stronger recirculation within the inner basin. As the inner basin freshens due to glacier meltwater, entrainment-driven inflow may further induce rapid draw-in of external waters from sill depth, with a corresponding increase in mixing around the sill (Hager et al., 2022). Therefore, by both enhancing horizontal velocities through recirculation and increasing heat through the drawing in of warm surface waters, plume-entrainment is expected to support further the argument that the inner sill is a potential contributor to the rapid retreat of Neumayer Glacier.

Though we do not believe the lack of plume-entrainment-driven inflow invalidates the present study; since Cumberland Bay's oceanography is distinct from that of other studies of this process (due to the warm over cold temperature structure), a greater understanding requires the use of a coupled model. We emphasize that the development of a coupled plume-ocean model will be pursued in future work.

5 Conclusions

This study combines observational data and a new validated high-resolution model of Cumberland Bay, South Georgia, to greatly enhance understanding of the oceanographic

variability and to provide insight into the drivers of glacier retreat. Observations show a strong seasonal cycle influenced by freshwater input, with interannual variability evident in austral summer and early winter, albeit weaker than the seasonal variability. Modeling results suggest that freshwater forcing via subglacial plumes is a key driver of both temporal and spatial variability. The difference in bathymetry between Cumberland Bay's two fjord arms, West Bay and East Bay, results in differing signals of buoyancy-driven outflow. The possible presence of a postulated inner sill in West Bay alters the seasonal variability in buoyancy-driven outflow and the properties within the resulting inner basin. We find evidence to suggest that the rapid retreat of Neumayer Glacier in West Bay, compared to Nordenskjöld Glacier in East Bay, might be explained by the trapping of warmer waters in the inner basin by a postulated shallow inner sill, with a possible positive feedback mechanism enhancing glacial melt and preventing restabilization of the glacier terminus. Further study is required to test this hypothesis through the acquisition of accurate bathymetric data over the inner sill in West Bay together with a coupled ice-ocean-atmosphere model at higher spatial resolution. With the use of the new model as a tool, future studies can identify other key drivers of variability in circulation and shelf exchange, as well as investigate interannual variability that may have triggered the retreat from the inner sill.

The fjord circulation patterns identified in this study have wider implications beyond glacier retreat. For example, the seasonality of buoyancy-driven outflow and the cross-fjord flow variability suggest the transport and retention of fish larvae will be sensitive to the timing and location of egg hatching. The availability of iron for downstream phytoplankton blooms derived from glacial flour plumes may be limited by a subsurface terminating plume or the presence of a sill acting as a barrier. This study is a fundamental step toward understanding the implications of oceanographic variability for glacier dynamics in Cumberland Bay, whilst providing a tool for investigating the impact of oceanographic variability on the marine ecosystem at South Georgia.

Acknowledgments

This work was supported by the Natural Environment Research Council via the BAS Polar Oceans program and the INSPIRE Doctoral Training Partnership. The authors would like to thank Polar Seafish Ltd for additional support and funding. We thank the Government of South Georgia and the South Sandwich Islands and the crew of the Pharos SG for facilitating and aiding CTD data collection. The numerical simulations were carried out on the ARCHER2 UK National Supercomputing Service (https://www.archer2.ac.uk/). The authors thank two reviewers, whose comments helped us improve the original manuscript.

Data availability statement

The data are currently available in the provided figures and tables. The observational data and model output underlying the figures and tables in this paper are in the process of being made available through the UK Polar Data Centre. The model code for NEMO-4.0.6 is available from the NEMO website (**www.nemo-ocean.eu**).

References

Bartholomaus, T. C., Stearns, L. A., Sutherland, D. A., Shroyer, E. L., Nash, J. D., Walker, R. T., Catania, G., Felikson, D., Carroll, D., Fried, M. J., Noël, B. P. Y., & Van Den Broeke, M. R. (2016). Contrasts in the response of adjacent fjords and glaciers to ice-sheet surface melt in West Greenland. *Annals of Glaciology*, *57*(73), 25–38. https://doi.org/10.1017/aog.2016.19

Benn, D., & Evans, D. J. A. (2014). Glaciers and Glaciation, Second Edition. In *Glaciers and Glaciation, Second Edition*. https://doi.org/10.4324/9780203785010

Benn, D. I., Cowton, T., Todd, J., & Luckman, A. (2017). Glacier Calving in Greenland. In *Current Climate Change Reports* (Vol. 3, Issue 4). https://doi.org/10.1007/s40641-017-0070-1

Berntsen, J., Xing, J., & Davies, A. M. (2009). *Numerical studies of flow over a sill : sensitivity of the non-hydrostatic effects to the grid size*. 1043–1059. https://doi.org/10.1007/s10236-009-0227-0

Boone, W., Rysgaard, S., Kirillov, S., Dmitrenko, I., Bendtsen, J., Mortensen, J., Meire, L., Petrusevich, V., & Barber, D. G. (2017). Circulation and fjord-shelf exchange during the ice-covered period in Young Sound-Tyrolerfjord, Northeast Greenland (74°N). *Estuarine, Coastal and Shelf Science*, *194*, 205–216. https://doi.org/10.1016/j.ecss.2017.06.021

Carroll, D., Sutherland, D. A., Shroyer, E. L., Nash, J. D., Catania, G. A., & Stearns, L. A. (2015). Modeling turbulent subglacial meltwater plumes: Implications for fjord-scale buoyancy-driven circulation. *Journal of Physical Oceanography*. https://doi.org/10.1175/JPO-D-15-0033.1

Catania, G. A., Stearns, L. A., Sutherland, D. A., Fried, M. J., Bartholomaus, T. C., Morlighem, M., Shroyer, E., & Nash, J. (2018). Geometric Controls on Tidewater Glacier Retreat in Central Western Greenland. *Journal of Geophysical Research: Earth Surface*, *123*(8), 2024–2038. https://doi.org/10.1029/2017JF004499

Christoffersen, P., Mugford, R. I., Heywood, K. J., Joughin, I., Dowdeswell, J. A., Syvitski, J. P. M., Luckman, A., & Benham, T. J. (2011). Warming of waters in an East Greenland fjord prior to glacier retreat: Mechanisms and connection to large-scale atmospheric conditions. *Cryosphere*. https://doi.org/10.5194/tc-5-701-2011

Chu, V. W. (2014). Greenland ice sheet hydrology: A review. *Progress in Physical Geography*, *38*(1). https://doi.org/10.1177/0309133313507075

Cook, A. J., Poncet, S., Cooper, A. P. R., Herbert, D. J., & Christie, D. (2010). Glacier retreat on South Georgia and implications for the spread of rats. *Antarctic Science*, *22*(3), 255–263. https://doi.org/10.1017/S0954102010000064

Cottier, F. R., Nilsen, F., Skogseth, R., Tverberg, V., Skardhamar, J., & Svendsen, H. (2010). Arctic fjords: A review of the oceanographic environment and dominant physical processes. *Geological Society Special Publication*, *344*(November), 35–50. https://doi.org/10.1144/SP344.4

768 Cowton, T., Slater, D., Sole, A., Goldberg, D., & Nienow, P. (2015). Modeling the impact of
769 glacial runoff on fjord circulation and submarine melt rate using a new subgrid-scale
770 parameterization for glacial plumes. *Journal of Geophysical Research: Oceans*.
771 https://doi.org/10.1002/2014JC010324

772 Cowton, T., Sole, A., Nienow, P., Slater, D., Wilton, D., & Hanna, E. (2016). Controls on the
773 transport of oceanic heat to Kangerdlugssuaq Glacier, East Greenland. *Journal of*
774 *Glaciology*, *62*(236). https://doi.org/10.1017/jog.2016.117

775 DAVIES, H. (1976). A lateral boundary formulation for multi-level prediction models. *Quarterly*
776 *Journal of the Royal Meteorological Society*, *102*(432). https://doi.org/10.1256/smsqj.43209

777 Davison, B. J., Cowton, T. R., Cottier, F. R., & Sole, A. J. (2020). Iceberg melting substantially
778 modifies oceanic heat flux towards a major Greenlandic tidewater glacier. *Nature*
779 *Communications*, *11*(1). https://doi.org/10.1038/s41467-020-19805-7

780 Egbert, G. D., & Erofeeva, S. Y. (2002). Efficient inverse modeling of barotropic ocean tides.
781 *Journal of Atmospheric and Oceanic Technology*. https://doi.org/10.1175/1520-
782 0426(2002)019<0183:EIMOBO>2.0.CO;2

783 ENGEDAHL, H. (1995). Use of the flow relaxation scheme in a three-dimensional baroclinic
784 ocean model with realistic topography. *Tellus A*, *47*(3). https://doi.org/10.1034/j.1600-
785 0870.1995.t01-2-00006.x

786 Everson, I. (1992). *M a n a g in g S o u th e rn O c e a n krill a n d fish stocks in a c h a n g in g e*
787 *n v iro n m e n t*. 311–317.

788 Everson, I., North, A. W., Paul, A., Cooper, R., McWilliam, N. C., & Kock, K. H. (2001).
789 Spawning locations of mackerel icefish at South Georgia. *CCAMLR Science*.

790 Flather, R. A. (1994). A storm surge prediction model for the northern Bay of Bengal with
791 application to the cyclone disaster in April 1991. *Journal of Physical Oceanography*, *24*(1).
792 https://doi.org/10.1175/1520-0485(1994)024<0172:ASSPMF>2.0.CO;2

793 Fraser, N. J., & Inall, M. E. (2018). Influence of Barrier Wind Forcing on Heat Delivery Toward
794 the Greenland Ice Sheet. *Journal of Geophysical Research: Oceans*, *123*(4), 2513–2538.
795 https://doi.org/10.1002/2017JC013464

796 Gade, H. G. (1979). Melting of Ice in Sea Water: A Primitive Model with Application to the
797 Antarctic Ice Shelf and Icebergs. *Journal of Physical Oceanography*, *9*(1).
798 https://doi.org/10.1175/1520-0485(1979)009<0189:moiisw>2.0.co;2

799 Gordon, J. E., Haynes, V. M., & Hubbard, A. (2008). Recent glacier changes and climate trends
800 on South Georgia. *Global and Planetary Change*, *60*(1–2), 72–84.
801 https://doi.org/10.1016/j.gloplacha.2006.07.037

802 Hager, A. O., Sutherland, D. A., Amundson, J. M., Jackson, R. H., Kienholz, C., Motyka, R. J.,
803 & Nash, J. D. (2022). Subglacial Discharge Reflux and Buoyancy Forcing Drive
804 Seasonality in a Silled Glacial Fjord. *Journal of Geophysical Research: Oceans*, *127*(5).
805 https://doi.org/10.1029/2021JC018355

806 Hersbach, H., Bell, B., Berrisford, P., Hirahara, S., Horányi, A., Muñoz-Sabater, J., Nicolas, J.,
807 Peubey, C., Radu, R., Schepers, D., Simmons, A., Soci, C., Abdalla, S., Abellan, X.,
808 Balsamo, G., Bechtold, P., Biavati, G., Bidlot, J., Bonavita, M., … Thépaut, J. N. (2020).
809 The ERA5 global reanalysis. *Quarterly Journal of the Royal Meteorological Society*,
810 *146*(730). https://doi.org/10.1002/qj.3803

811 Hewitt, I. J. (2020). Subglacial Plumes. *Annual Review of Fluid Mechanics*, *52*(1), 145–169.
812 https://doi.org/10.1146/annurev-fluid-010719-060252

813 Hodgson, D. A., Graham, A. G. C., Grif, H. J., Roberts, S. J., Cofaigh, C. Ó., Bentley, M. J., &
814 Evans, D. J. A. (2014). *Glacial history of sub-Antarctic South Georgia based on the*
815 *submarine geomorphology of its fjords q*. *89*, 129–147.
816 https://doi.org/10.1016/j.quascirev.2013.12.005

817 Hogg, O. T., Huvenne, V. A. I., Griffiths, H. J., Dorschel, B., & Linse, K. (2016). Landscape
818 mapping at sub-Antarctic South Georgia provides a protocol for underpinning large-scale
819 marine protected areas. *Scientific Reports*, *6*. https://doi.org/10.1038/srep33163

820 Holland, D. M., & Jenkins, A. (1999). Modeling thermodynamic ice-ocean interactions at the
821 base of an ice shelf. *Journal of Physical Oceanography*, *29*(8 PART 1).
822 https://doi.org/10.1175/1520-0485(1999)029<1787:mtioia>2.0.co;2

Hollingsworth, A., Kållberg, P., Renner, V., & Burridge, D. M. (1983). An internal symmetric computational instability. *Quarterly Journal of the Royal Meteorological Society*, *109*(460). https://doi.org/10.1002/qj.49710946012

Holmes, T. M., Wuttig, K., Chase, Z., Schallenberg, C., van der Merwe, P., Townsend, A. T., & Bowie, A. R. (2019). Glacial and hydrothermal sources of dissolved iron(II) in Southern Ocean waters surrounding Heard and McDonald Islands. In *In Prep.* (Issue Ii). https://doi.org/10.1029/2020JC016286

Holt, J. T., Allen, J. I., Proctor, R., & Gilbert, F. (2005). Error quantification of a high-resolution coupled hydrodynamic-ecosystem coastal-ocean model: Part 1 model overview and assessment of the hydrodynamics. *Journal of Marine Systems*, *57*(1–2). https://doi.org/10.1016/j.jmarsys.2005.04.008

Jackson, R. H., Shroyer, E. L., Nash, J. D., Sutherland, D. A., Carroll, D., Fried, M. J., Catania, G. A., Bartholomaus, T. C., & Stearns, L. A. (2017). Near-glacier surveying of a subglacial discharge plume: Implications for plume parameterizations. *Geophysical Research Letters*. https://doi.org/10.1002/2017GL073602

Jenkins, A. (2011). Convection-driven melting near the grounding lines of ice shelves and tidewater glaciers. *Journal of Physical Oceanography*. https://doi.org/10.1175/JPO-D-11-03.1

Large, W. G., & Yeager, S. G. (2004). Diurnal to decadal global forcing for ocean and sea-ice models: the data sets and flux climatologies. *Ech. Rep., NCAR Climate and Global Dynamics Division; Boulder, CO, United States*.

Lin, P., Pickart, R. S., Torres, D. J., & Pacini, A. (2018). Evolution of the freshwater coastal current at the Southern Tip of Greenland. *Journal of Physical Oceanography*, *48*(9). https://doi.org/10.1175/JPO-D-18-0035.1

Luckman, A., Benn, D. I., Cottier, F., Bevan, S., Nilsen, F., & Inall, M. (2015). Calving rates at tidewater glaciers vary strongly with ocean temperature. *Nature Communications*, *6*. https://doi.org/10.1038/ncomms9566

Meredith, M. P., Brandon, M. A., Murphy, E. J., Trathan, P. N., Thorpe, S. E., Bone, D. G., Chernyshkov, P. P., & Sushin, V. A. (2005). Variability in hydrographic conditions to the

east and northwest of South Georgia, 1996-2001. *Journal of Marine Systems*. https://doi.org/10.1016/j.jmarsys.2004.05.005

Millan, R., Rignot, E., Mouginot, J., Wood, M., Bjørk, A. A., & Morlighem, M. (2018). Vulnerability of Southeast Greenland Glaciers to Warm Atlantic Water From Operation IceBridge and Ocean Melting Greenland Data. *Geophysical Research Letters*, *45*(6). https://doi.org/10.1002/2017GL076561

Millgate, T., Holland, P. R., Jenkins, A., & Johnson, H. L. (2013). The effect of basal channels on oceanic ice-shelf melting. *Journal of Geophysical Research: Oceans*, *118*(12). https://doi.org/10.1002/2013JC009402

Mortensen, J., Bendtsen, J., Lennert, K., & Rysgaard, S. (2014). Seasonal variability of the circulation system in a west Greenland tidewater outlet glacier fjord, Godthåbsfjord (64°N). *Journal of Geophysical Research: Earth Surface*, *119*(12). https://doi.org/10.1002/2014JF003267

Mortensen, J., Bendtsen, J., Motyka, R. J., Lennert, K., Truffer, M., Fahnestock, M., & Rysgaard, S. (2013). On the seasonal freshwater stratification in the proximity of fast-flowing tidewater outlet glaciers in a sub-Arctic sill fjord. *Journal of Geophysical Research: Oceans*, *118*(3). https://doi.org/10.1002/jgrc.20134

Mortensen, J., Lennert, K., Bendtsen, J., & Rysgaard, S. (2011). Heat sources for glacial melt in a sub-Arctic fjord (Godthåbsfjord) in contact with the Greenland Ice Sheet. *Journal of Geophysical Research: Oceans*, *116*(1), 1–13. https://doi.org/10.1029/2010JC006528

Motyka, R. J., Cassotto, R., Truffer, M., Kjeldsen, K. K., As, D. Van, Korsgaard, N. J., Fahnestock, M., Howat, I., Langen, P. L., Mortensen, J., Lennert, K., & Rysgaard, S. (2017). Asynchronous behavior of outlet glaciers feeding Godthåbsfjord (Nuup Kangerlua) and the triggering of Narsap Sermia's retreat in SW Greenland. *Journal of Glaciology*, *63*(238). https://doi.org/10.1017/jog.2016.138

Okubo, A. (1971). Oceanic diffusion diagrams. *Deep Sea Research and Oceanographic Abstracts*, *18*(8), 789–802. https://doi.org/10.1016/0011-7471(71)90046-5

O'Leary, M., & Christoffersen, P. (2013). Calving on tidewater glaciers amplified by submarine frontal melting. *Cryosphere*. https://doi.org/10.5194/tc-7-119-2013

881 Oliver, H., Castelao, R. M., Wang, C., & Yager, P. L. (2020). Meltwater-Enhanced Nutrient
882 Export From Greenland's Glacial Fjords: A Sensitivity Analysis. *Journal of Geophysical*
883 *Research: Oceans*, *125*(7). https://doi.org/10.1029/2020JC016185

884 Orsi, A. H., Whitworth, T., & Nowlin, W. D. (1995). On the meridional extent and fronts of the
885 Antarctic Circumpolar Current. *Deep-Sea Research Part I*, *42*(5).
886 https://doi.org/10.1016/0967-0637(95)00021-W

887 Park, J. W., Gourmelen, N., Shepherd, A., Kim, S. W., Vaughan, D. G., & Wingham, D. J.
888 (2013). Sustained retreat of the Pine Island Glacier. *Geophysical Research Letters*, *40*(10).
889 https://doi.org/10.1002/grl.50379

890 Penduff, T., Le Sommer, J., Barnier, B., Treguier, A. M., Molines, J. M., & Madec, G. (2007).
891 Influence of numerical schemes on current-topography interactions in 1/4° global ocean
892 simulations. *Ocean Science*, *3*(4). https://doi.org/10.5194/os-3-509-2007

893 Schaffer, J., Kanzow, T., von Appen, W. J., von Albedyll, L., Arndt, J. E., & Roberts, D. H.
894 (2020). Bathymetry constrains ocean heat supply to Greenland's largest glacier tongue.
895 *Nature Geoscience*, *13*(3). https://doi.org/10.1038/s41561-019-0529-x

896 Sciascia, R., Straneo, F., Cenedese, C., & Heimbach, P. (2013). *Seasonal variability of*
897 *submarine melt rate and circulation in an East Greenland fjord*. *118*(May), 2492–2506.
898 https://doi.org/10.1002/jgrc.20142

899 Silvano, A., Rintoul, S. R., Peña-Molino, B., & Williams, G. D. (2017). Distribution of water
900 masses and meltwater on the continental shelf near the Totten and Moscow University ice
901 shelves. *Journal of Geophysical Research: Oceans*, *122*(3).
902 https://doi.org/10.1002/2016JC012115

903 Slater, D. A., Nienow, P. W., Cowton, T. R., Goldberg, D. N., & Sole, A. J. (2015). Effect of
904 near-terminus subglacial hydrology on tidewater glacier submarine melt rates. *Geophysical*
905 *Research Letters*, *42*(8). https://doi.org/10.1002/2014GL062494

906 Slater, D. A., Nienow, P. W., Goldberg, D. N., Cowton, T. R., & Sole, A. J. (2017). A model for
907 tidewater glacier undercutting by submarine melting. *Geophysical Research Letters*.
908 https://doi.org/10.1002/2016GL072374

Sommer, U., & Lengfellner, K. (2008). Climate change and the timing, magnitude, and composition of the phytoplankton spring bloom. *Global Change Biology*. https://doi.org/10.1111/j.1365-2486.2008.01571.x

Soontiens, N., & Allen, S. E. (2017). Modelling sensitivities to mixing and advection in a sill-basin estuarine system. *Ocean Modelling*, *112*, 17–32. https://doi.org/10.1016/j.ocemod.2017.02.008

Soontiens, N., Allen, S. E., Latornell, D., Le Souëf, K., MacHuca, I., Paquin, J. P., Lu, Y., Thompson, K., & Korabel, V. (2016). Storm Surges in the Strait of Georgia Simulated with a Regional Model. *Atmosphere - Ocean*, *54*(1), 1–21. https://doi.org/10.1080/07055900.2015.1108899

Staalstrøm, A., & Petter, L. (2016). Vertical mixing and internal wave energy fluxes in a sill fjord. *Journal of Marine Systems*, *159*, 15–32. https://doi.org/10.1016/j.jmarsys.2016.02.005

Straneo, F., & Cenedese, C. (2015). The dynamics of greenland's glacial fjords and their role in climate. *Annual Review of Marine Science*, *7*. https://doi.org/10.1146/annurev-marine-010213-135133

Straneo, F., Curry, R. G., Sutherland, D. A., Hamilton, G. S., Cenedese, C., Våge, K., & Stearns, L. A. (2011). Impact of fjord dynamics and glacial runoff on the circulation near Helheim Glacier. *Nature Geoscience*. https://doi.org/10.1038/ngeo1109

Straneo, F., Hamilton, G. S., Sutherland, D. A., Stearns, L. A., Davidson, F., Hammill, M. O., Stenson, G. B., & Rosing-asvid, A. (2010). Rapid circulation of warm subtropical waters in a major glacial fjord in East Greenland. *Nature Geoscience*, *3*(February). https://doi.org/10.1038/ngeo764

Umlauf, L., & Burchard, H. (2003). A generic length-scale equation for geophysical turbulence models. *Journal of Marine Research*, *61*(2). https://doi.org/10.1357/002224003322005087

Venables, H. J., Meredith, M. P., & Brearley, J. A. (2017). Modification of deep waters in Marguerite Bay, western Antarctic Peninsula, caused by topographic overflows. *Deep-Sea Research Part II: Topical Studies in Oceanography*, *139*. https://doi.org/10.1016/j.dsr2.2016.09.005

Ward, P. (1989). The distribution of zooplankton in an Antarctic fjord at South Georgia during summer and winter. *Antarctic Science*, *1*(2). https://doi.org/10.1017/S0954102089000210

Wesławski, J. M., Kendall, M. A., Włodarska-Kowalczuk, M., Iken, K., Kedra, M., Legezynska, J., & Sejr, M. K. (2011). Climate change effects on Arctic fjord and coastal macrobenthic diversity-observations and predictions. In *Marine Biodiversity* (Vol. 41, Issue 1). https://doi.org/10.1007/s12526-010-0073-9

Węsławski, J. M., Pedersen, G., Petersen, S. F., & Poraziński, K. (2000). Entrapment of macroplankton in an Arctic fjord basin, Kongsfjorden, Svalbard. *Oceanologia*, *42*(1), 57–69.

Winder, M., & Sommer, U. (2012). Phytoplankton response to a changing climate. In *Hydrobiologia*. https://doi.org/10.1007/s10750-012-1149-2

Young, E. F., Meredith, M. P., Murphy, E. J., & Carvalho, G. R. (2011). High-resolution modelling of the shelf and open ocean adjacent to South Georgia, Southern Ocean. *Deep-Sea Research Part II: Topical Studies in Oceanography*, *58*(13–16). https://doi.org/10.1016/j.dsr2.2009.11.003

Young, E. F., Thorpe, S. E., Banglawala, N., & Murphy, E. J. (2014). Variability in transport pathways on and around the South Georgia shelf, Southern Ocean: Implications for recruitment and retention. *Journal of Geophysical Research: Oceans*, *119*(1), 241–252. https://doi.org/10.1002/2013JC009348

Young, E., Murphy, E., & Trathan, P. (2016). High-resolution ocean modelling of the South Georgia and South Orkney Islands regions. *WG-EMM-16/15. CCAMLR Working Group on Ecosystem Monitoring and Management. Report of the XXXV Scientific Committee, Bologna, Italy.*

Zhao, K. X., Stewart, A. L., McWilliams, J. C., Fenty, I. G., & Rignot, E. J. (2023). Standing Eddies in Glacial Fjords and Their Role in Fjord Circulation and Melt. *Journal of Physical Oceanography*, *53*(3). https://doi.org/10.1175/JPO-D-22-0085.1

Figure 1.

a)

Polar Front (PF)
Southern ACC Front (SACCF)

48°S
50°S
52°S
54°S
56°S
58°S
60°S
Longitude
50°W
45°W
40°W
35°W
30°W
25°W
Latitude

b)

12'
15'
54°S
18.00'
21'
42'
36'
36°W
30.00'
24'
18'
Latitude

c)

54°S
6'
12'
18'
24'
Longitude
48'
36'
24'
12'
36°W
Latitude

Partially eroded outer sill
Neumayer Glacier terminus
West Bay
Outer sill
East Bay
KEP
Estimated position of shallow inner sill
Inner sill
Nordenskjöld Glacier terminus

300
250
200
150
100
50
0 m

Figure 2.

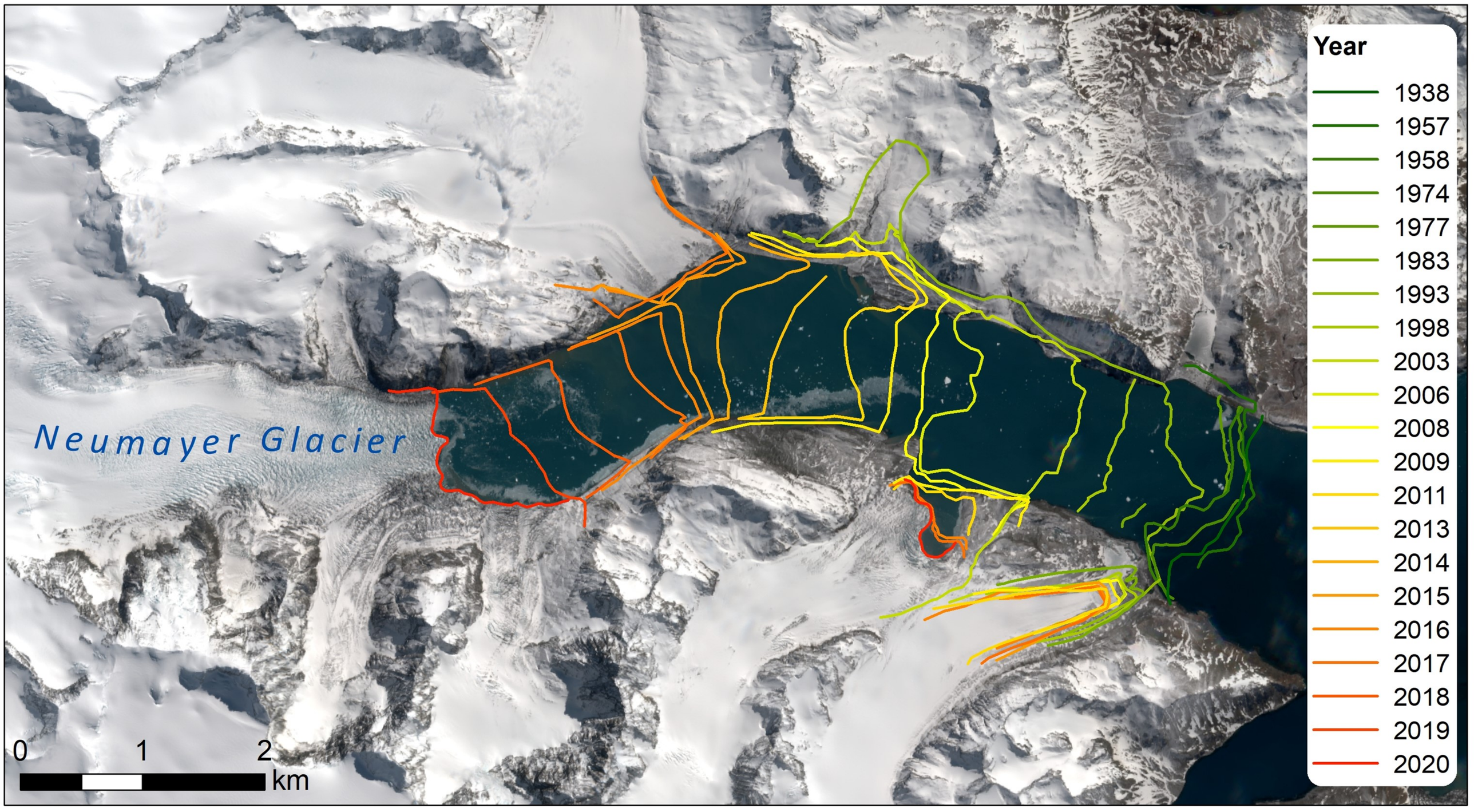
Neumayer Glacier
0
1
2
km
Year
1938
1957
1958
1974
1977
1983
1993
1998
2003
2006
2008
2009
2011
2013
2014
2015
2016
2017
2018
2019
2020

Figure 3.

a) Q_S m^3s^{-1}

40
30
20
10

WB
EB
WB SILL

b) T °C

4
2
0

c) S

34
33.5
33

d) Q_P m^3s^{-1}

2000
1000
0

Nov Feb May Aug

e) D m

0
50
100

Nov Feb May Aug

Figure 4.

a)

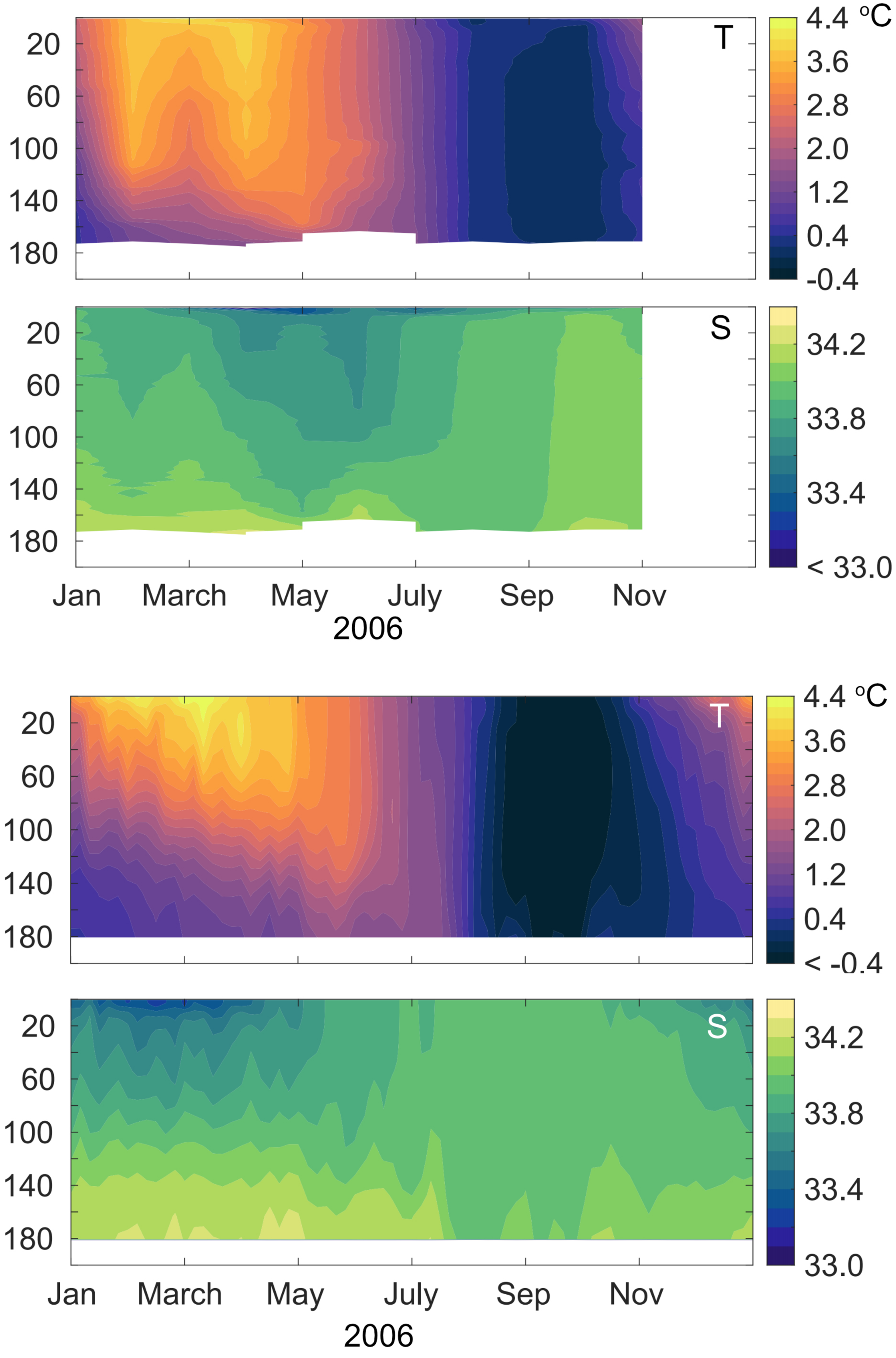
Depth, m
20
60
100
140
180
T
4.4 °C
3.6
2.8
2.0
1.2
0.4
-0.4
S
34.2
33.8
33.4
< 33.0
Jan
March
May
July
Sep
Nov
2006

b)

Depth, m
20
60
100
140
180
T
4.4 °C
3.6
2.8
2.0
1.2
0.4
< -0.4
S
34.2
33.8
33.4
33.0
Jan
March
May
July
Sep
Nov
2006

Figure 5.

WB
EB
a)
Depth, m
50
150
250
Nov: T
3.8 °C
2.2
0.6
Nov: S
34.2
33.4
32.6
b)
Feb: T
4.4 °C
3.2
2.0
0.8
Feb: S
34.4
33.6
32.8
32.0
c)
Apr: T
3.2 °C
2.4
1.6
Apr: S
34.4
33.6
32.8
-20
-10
0
10
20
Distance along transect, km

Figure 6.

November
February
April

a)
b)
runoff line
melt line
25.6954
26.1136
26.5318
26.95
25.7973
26.2029
26.6086
27.0143
27.42
15 m
50 m
200 m
near sill
WB
EB
Conservative Temperature, °C
Absolute Salinity, g kg^{-1}

Figure 7.

February
June
October
2004
2005
2006
Depth, m
0
50
100
150
200
0
2
4
Conservative Temperature, °C
February
June
October
Depth, m
0
50
100
150
200
33
34
Absolute Salinity, g kg^{-1}

Figure 8.

a) Surface flows

b) 100 m flows

c) Sea surface temperature

November

February

May

August

latitude

12'
15'
54°S
18'
21'

42' 36' 36°W 24' 18'
30'

longitude

0 0.05 >0.1 ms^{-1}

0 0.025 > 0.05 ms^{-1}

< 0 1 2 3 > 4 °C

Figure 9.

-50 0 50 m^3s^{-1}

N **WB** S

W **EB** E

Depth, m

50
100
150

November

February

May

August

0 1 2

Distance, km

Figure 10.

a)

Depth, m

20
60
100
140

PLUME

WB

NOPLUME

WB

200
0
-200

m^3s^{-1}

Oct
Dec
Feb
April
June
Aug

b)

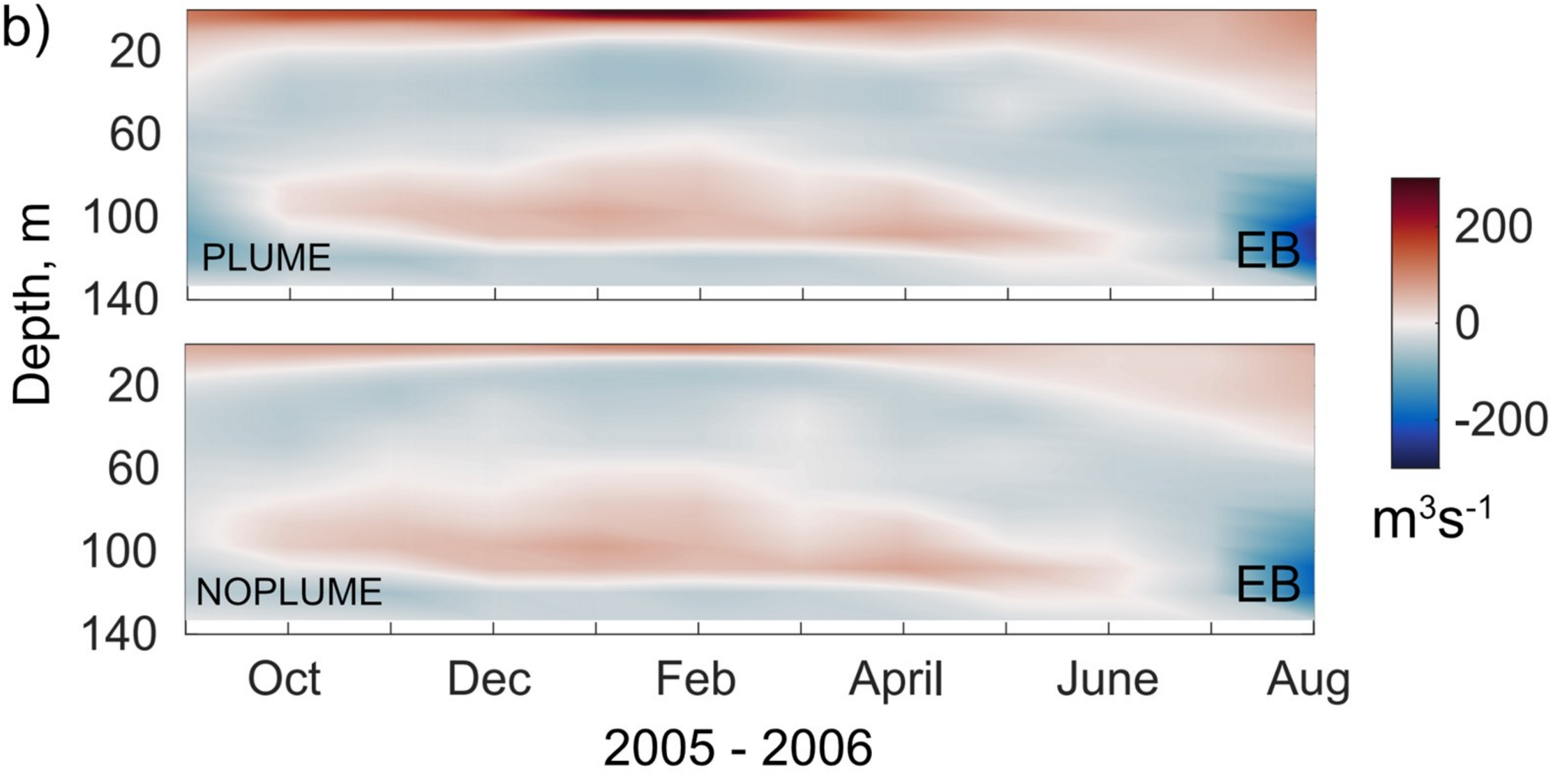

Figure 11.

a)

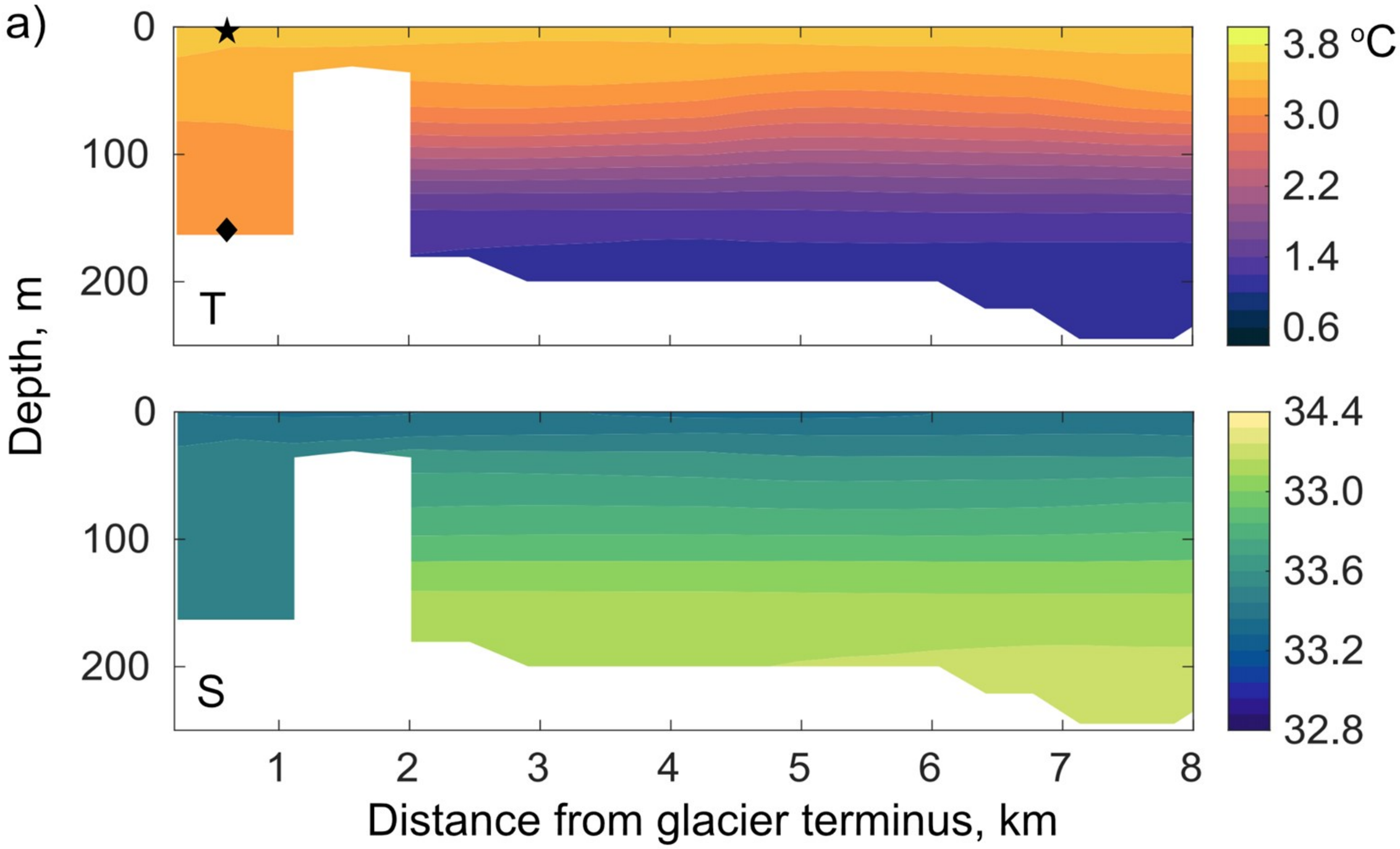
0
100
200
Depth, m
T
S
3.8 °C
3.0
2.2
1.4
0.6
34.4
33.0
33.6
33.2
32.8
1
2
3
4
5
6
7
8
Distance from glacier terminus, km

b)

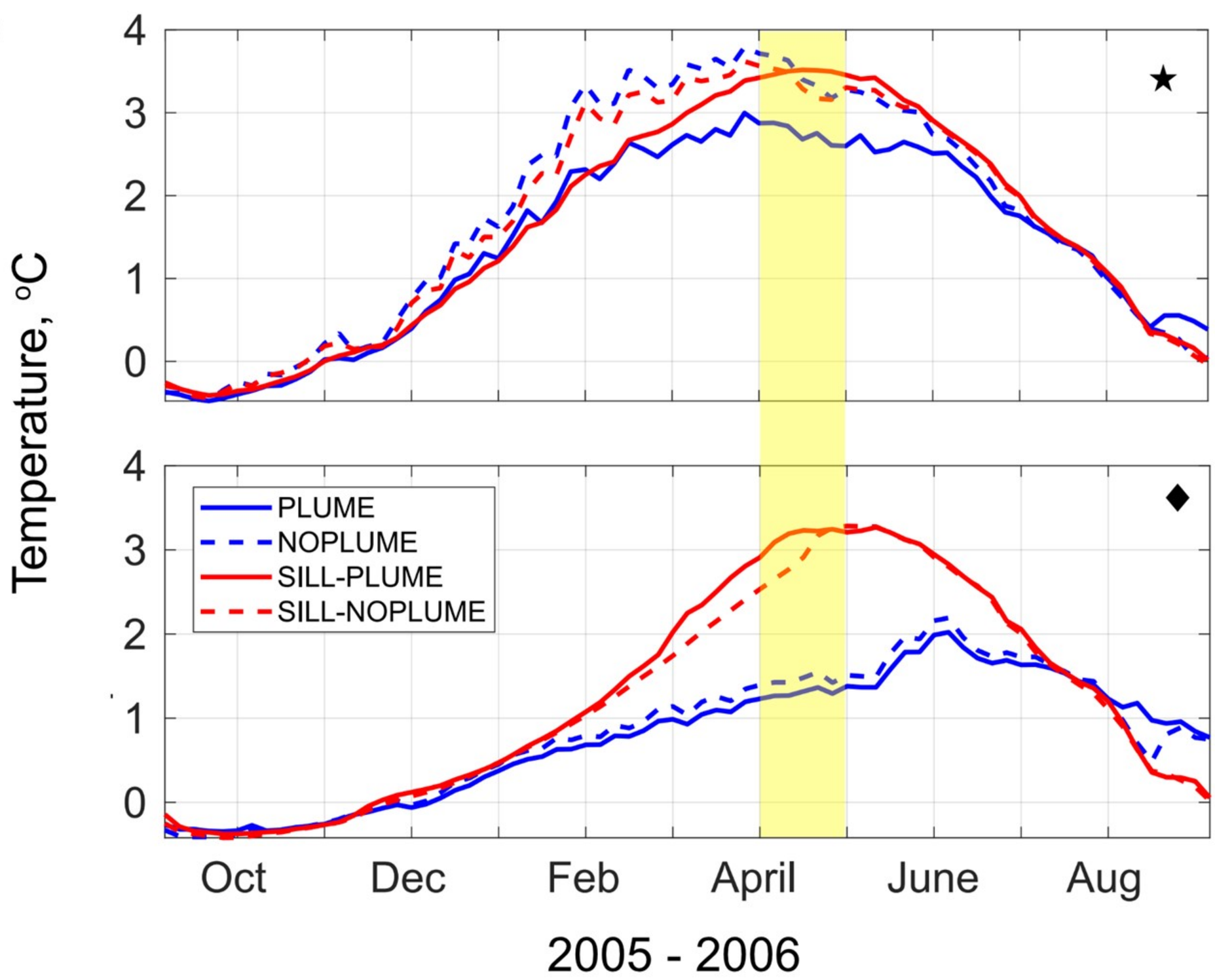
Temperature, °C
4
3
2
1
0
PLUME
NOPLUME
SILL-PLUME
SILL-NOPLUME
Oct
Dec
Feb
April
June
Aug
2005 - 2006

Figure 12.

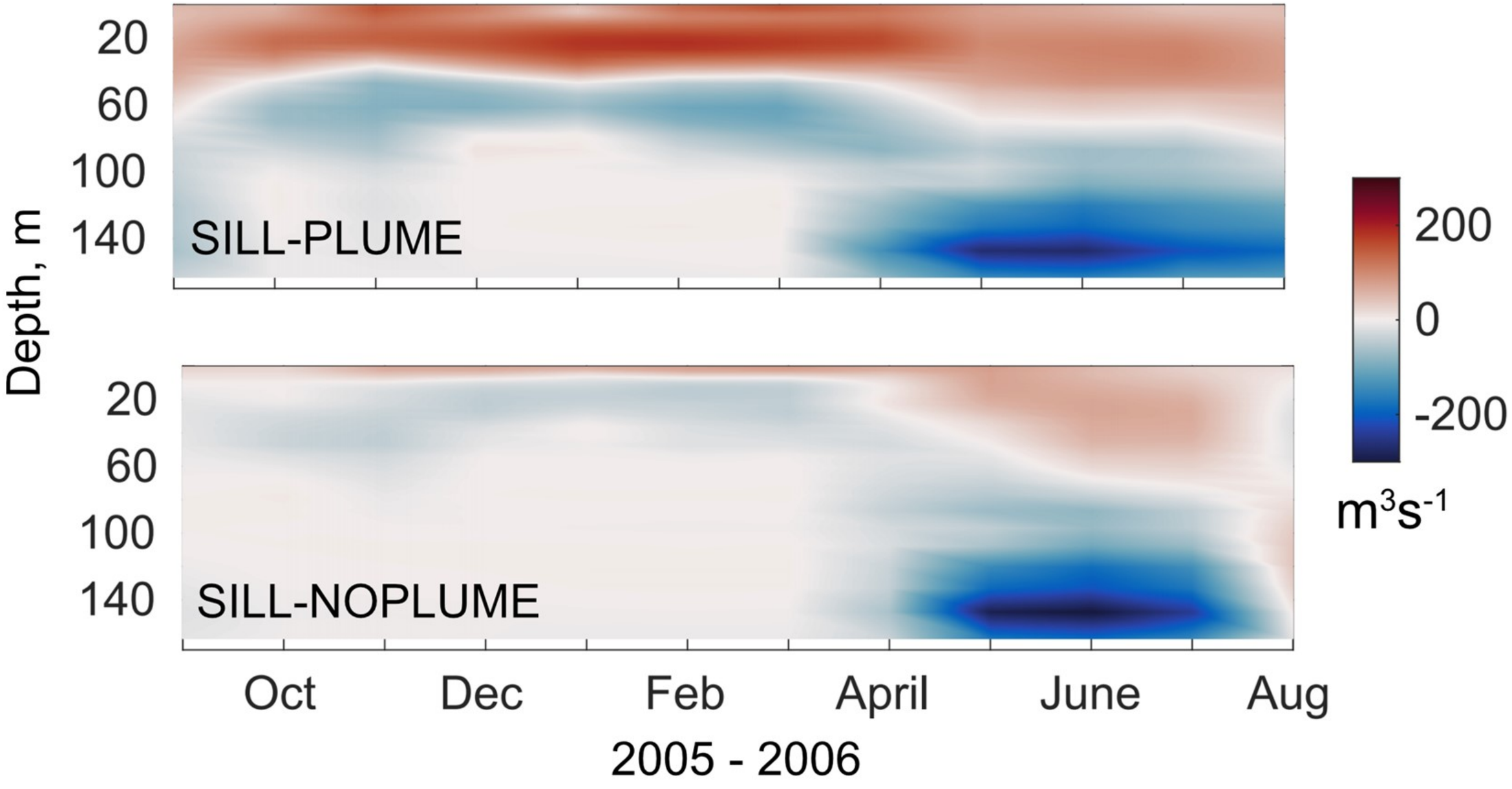
Depth, m
20
60
100
140
SILL-PLUME
20
60
100
140
SILL-NOPLUME
Oct
Dec
Feb
April
June
Aug
2005 - 2006
200
0
-200
m3s-1